Meson photoproduction on the proton using the BGO-OD detector complemented by a new Scintillating Ring (SciRi)

Georg Scheluchin

Masterarbeit in Physik
angefertigt im Physikalischen Institut

vorgelegt der
Mathematisch-Naturwissenschaftlichen Fakultät
der
Rheinischen Friedrich-Wilhelms-Universität
Bonn

August 2015

I hereby declare that this thesis was formulated by myself and that no sources or tools other than those cited were used.

Bonn, ...
Date Signature

1. Gutachter: Prof. Hartmut Schmieden
2. Gutachter: Prof. Philip L. Cole

Contents

CHAPTER 1

Introduction

It is an accepted fact that the positive charge of an atom is concentrated in the centre. This positive charge has its origin in the protons, which together with the neutral charged neutrons form a nucleus. An atom is, simply put, a nucleus surrounded by a cloud of electrons. Electrons are elementary particles with a negative charge. By excitation of the electrons, it is possible to separate the nucleus from the electrons. The nucleus itself is formed of individual nucleons. A nucleon – proton or neutron – further has a substructure, which is formed of quarks and gluons.
Quarks and gluons, together with the electrons, are part of the Standard Model. This model attempts to describe the fundamental interaction between particles. Particles which are part of this model are illustrated in figure 1.1. Within a constituent quarks model, the main difference between a proton and a neutron are their valence quarks. The proton consists of two up and one down quark with a charge sum of +1, while the neutron has one up and two down quarks. Particles composed out of three valence quarks are called baryons. A meson is a particle formed of a quark-antiquark pair. Such states composed of quarks are termed hadrons. The Δ^{++} baryon was subsequently discovered and has 3-up quarks with parallel spin. This arrangement contradicted the Pauli principle, which states that identical particles cannot occupy the same quantum state. The solution to this problem was the introduction of colour charge for quarks and gluons. This charge is an additional quantum number, but it does not represent a visual colour. While the electrostatic charge has two states, positive or negative, the colour charge has more charge states. It can be green, blue, red or a complementary colour to them. A Δ^{++} baryon would have a green, red and blue up quark, which now does not contradict the Pauli principle. By mixing the colours additive together they produce a white colour state. Colour charge is conserved as long a colourless state is formed. This means the quarks in a baryon have the colour green, red, blue or anti-green, anti-blue, anti-red. A meson than has a colour and its anti-colour to conserve colour charge. The colour charge is also used to explain why a free quark is not observable, as it can never have a colourless state alone. This means quarks are confined in a hadron. Up

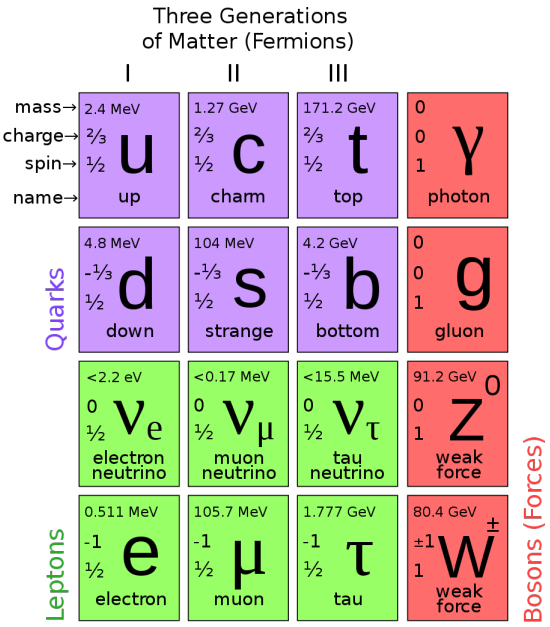

Figure 1.1: Particles of the Standard Model [1]

to now there is no generally agreed-upon explanation to this, so experiments to investigate the hadron structure are still present today.
The attempt to free a quark from a hadron using a high energy particle (such as a photon) results in additional production of hadrons. As the quark starts to be separated from the other quarks, energy is stored in the gluon binding. At a certain distance this binding has stored enough energy to produce a quark and anti-quark pair. These bind to the removed quark and the remaining quarks within the baryon to produce a colourless meson and baryon in the final state.

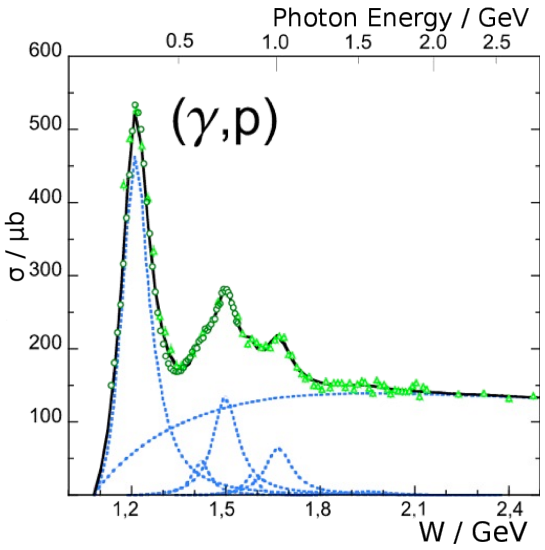

Figure 1.2: Total cross section of photon-proton reaction [2]

This prevents us from removing the constituents from the proton, so we try to investigate the bound gluon and quark system itself. As they form a bound quantum mechanical system, they possesses excitation levels. In principle, it is similar to atom spectroscopy and therefore it is possible to excite the nucleon to investigate this bound system. By using photons to excite the proton, one can measure a cross section which is shown in figure 1.2. Nucleon resonances are shown on top of a continuum, which overlap and interfere in energy and angle. To further investigate these resonances, one needs to disentangle each contributing resonance. One tool to disentangled those overlapping states is by meson photoproduction. The decay of a nucleon resonance proceeds mostly by means of producing final-state mesons. By reconstructing the mesons, it is possible to select a part of the total cross section.
Mesons are formed out of gluons and two valence quarks. Free mesons decay after a short amount of time into multiple particles. To reconstruct the meson a detector system, which can detect multiple charged and uncharged particles, is necessary. BGO-OD is one such detector which is focused on meson photoproduction and described in detail in chapter 2. The goal of this thesis was the reconstruction of mesons using the BGO-OD detector. On sample reactions delineated in chapter 3 it is shown that the BGO-OD detector has an acceptance hole in a critical region. To cover this acceptance gap, a new Scintillating Ring (SciRi) detector was constructed in the course of this thesis project, which now complements BGO-OD. The SciRi detector has three segmented scintillator rings with individual Avalanche Photodiode readout. The construction and commissioning of the SciRi detector are described in chapter 4. With the support from colleagues in the Crystal Barrel experiment, it was possible to complete this detector within half a year. The detector provides angle information for charged particles.
Having a detector system that detects particles is the first step towards meson reconstruction. Energy is deposited as particle pass through materials. In a segmented detector one particle can deposit energy in multiple segments. It is than necessary to reconstruct the particles energy and direction by forming clusters from individual detector hits. A photon deposits its energy in the material by developing an electromagnetic shower. Through the process of pair production, Compton scattering, bremsstrahlung and electron-positron annihilation the number of particles inside the shower increases. If two photons now hit the segmented detector at the same time and are in close proximity, their electromagnetic showers will overlap. This means that an energy deposition is spread over an large area in the segmented detector,

where now the problem arises to reconstruct the two photon momenta. Of course, this reconstruction also needs to be automated. In this case, we use a clustering algorithm. Development of different clustering methods are described in section 5.1.1. With these formed clusters, the particle tracks can be reconstructed. Additional detectors can also be used to determine the energy, charge or the mass of the particle. It is also possible to calculate these physical values through use of conservation laws, making it possible to reconstruct the final state of a reaction completely. Because many mesons decay into similar particles, it is necessary to reconstruct the mass of the parent meson for identification. Meson reconstruction is done for some selected mesons, as will be described in chapter 5.

CHAPTER 2

Experiment

To investigate meson photoproduction, the nucleon first needs to be excited with a photon. While only some few eV are needed to excite an atom, energies in the region of GeV are necessary for the nucleon. The Electron Stretcher Accelerator (ELSA) is used to produce photons of such a magnitude. ELSA accelerates electrons to energies of up to 3.2 GeV. The electron beam then enters the BGO-OD detector. After hitting a thin radiator, a real photon beam is produced via bremsstrahlung. After that the bremsstrahlung photons hit a target cell, which is typically filled with liquid hydrogen, acting as a target of free protons. The decay particles of the reaction are then detected with the BGO-OD detector setup, which is situated around the target cell.

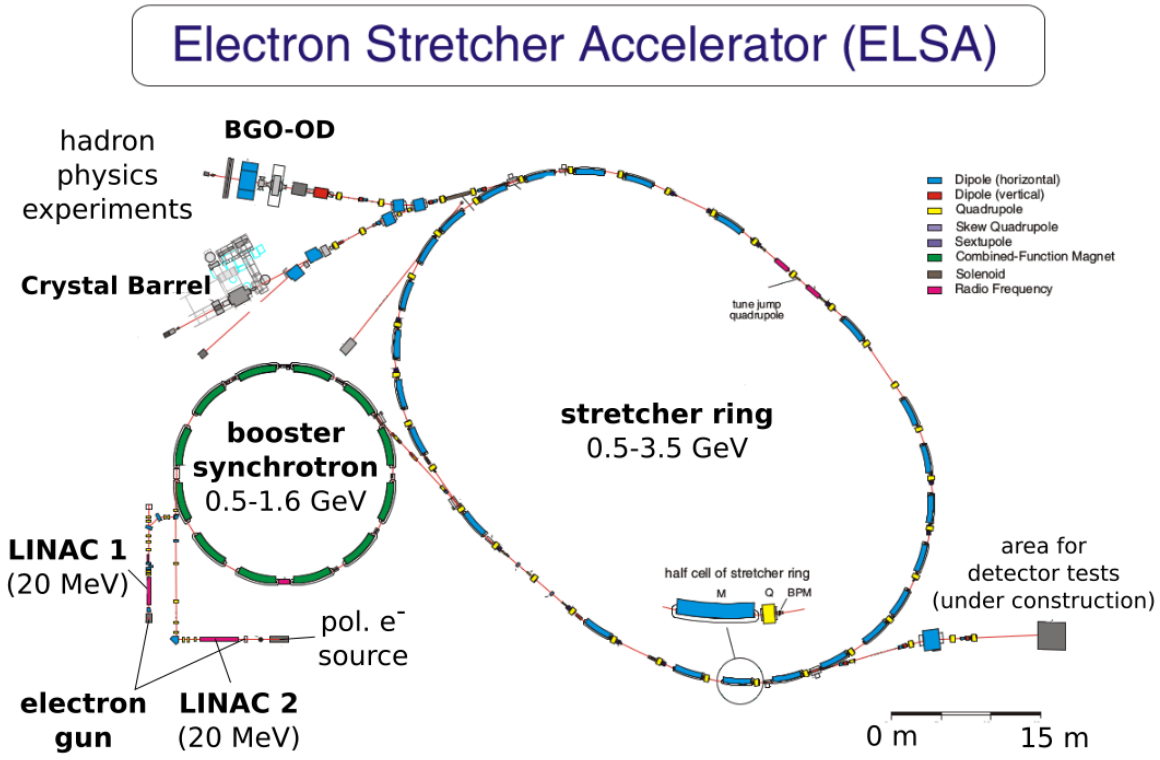

Figure 2.1: Overview of the Electron Stretcher Accelerator [3]

2.1 Electron Stretcher Accelerator (ELSA)

The Electron Stretcher Accelerator (ELSA) is located beneath the Physikalisches Institut building at the university of Bonn. The facility can be seen in figure 2.1. In the first stage, a thermal gun releases the electrons bound in the cathode material. A potential difference then removes and accelerates the electrons away from the cathode. With the linear accelerator LINAC these electrons gain an energy of approximately 20 MeV before they are inserted into the booster synchrotron. After an acceleration to at least 0.5 GeV, the electrons are guided into the stretcher ring where they can be accelerated up to 3.2 GeV.
The stretcher ring is filled in bunches by the booster synchrotron. The next step in accelerating the electrons to a higher energy begins once the stretcher ring is completely filled. As soon the electrons reach the required energy, a small part of the beam is extracted and then is directed to either the Crystal Barrel or the BGO-OD experiment. This leads to a quasi constant beam at the experiments. This process continues until the stretcher ring is completely depleted. The filling of the stretcher ring by the booster synchrotron then starts anew.
It is possible to accelerate linear polarised electrons for a circular polarised photon beam. In this case the electrons are polarised vertically so that they do not lose their polarisation during the acceleration in the circular accelerator. Just before the experiment the spin direction is turned by 90° into the horizontal plane.

2.2 BGO-OD experiment

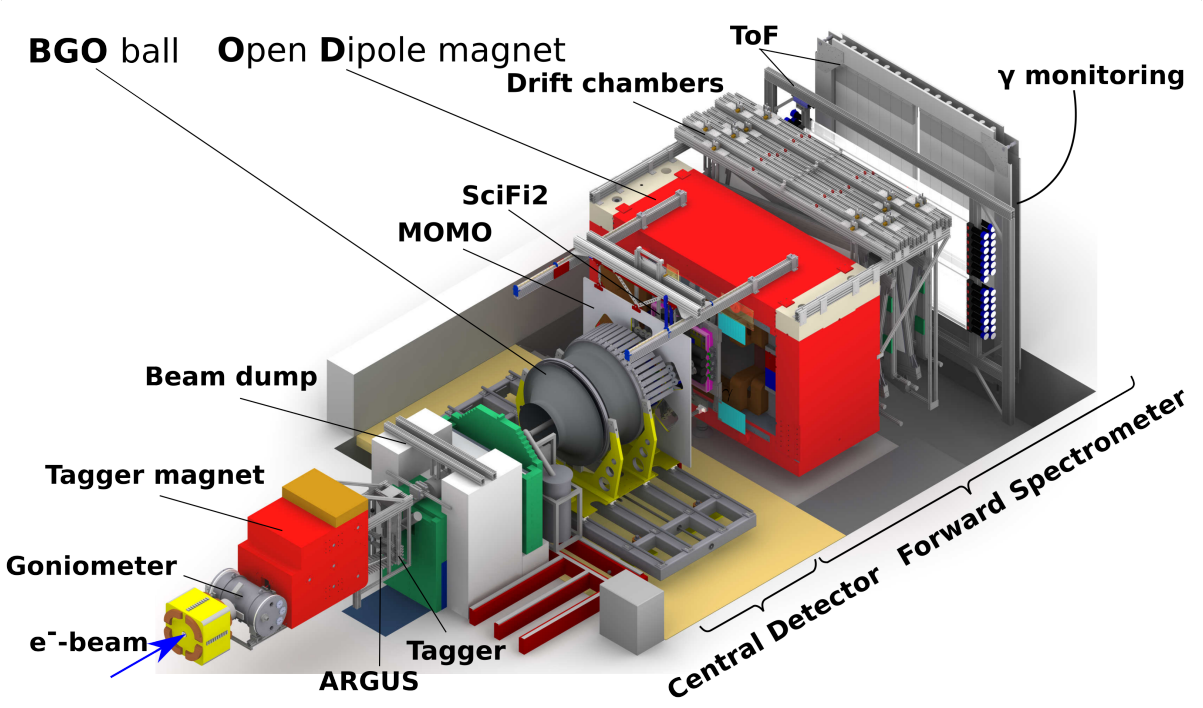

Figure 2.2: Overview of the BGO-OD experiment [4]

The BGO-OD experiment, located at the ELSA facility, was constructed by an international collaboration and is ideally suited to pursue meson photoproduction. An overview of the experiment is depicted in figure 2.2. The electron beam, which is provided by the ELSA accelerator, hits a radiator inside the goniometer. A real photon beam is then produced via bremsstrahlung. With the goniometer, it is possible to select a variety of radiators. For producing unpolarised photons one can choose from three different copper radiators, i.e. 50 μm, 150 μm or 200 μm. For producing linearly polarised photons a diamond radiator of thickness 500 μm is used. And for making circular polarised photons, an longitudinal polarised electron beam is directed into a ferromagnetic foil. Through helicity transfer, circularly polarised photons are produced. The ferromagnetic foil is needed to determine the degree of polarisation. The electrons in the beam can undergo Møller scattering with the electrons in the foil. An applied magnetic field polarises the outer shell electrons in the ferromagnetic foil. The cross section then has an asymmetry for symmetrical Møller scattering in parallel and anti-parallel electron spin configuration, due to the Pauli principle. This can be used to determine the polarisation degree. In this thesis project unpolarised photons were used to reconstruct mesons.
For this thesis polar coordinates will be used frequently to describe a direction in space. A particle moving in same direction as the beam goes in forward direction and will have a θ angle of 0°. Particles moving opposite the beam direction will have a θ angle of 180°. By looking in beam direction parallel to the floor, particles which are left to the beam have a ϕ angle of 0° and right to the beam 180°/ − 180°. In beam direction perpendicular to the floor, particles above the beam have $\phi = 90°$ and below the beam line $\phi = 270°/ - 90°$.

2.2.1 Photon tagging system (Tagger)

The bremsstrahlung photon produced in the goniometer radiator and the associated post-bremsstrahlung electron then enter the Tagger magnet. Here the electrons are deflected due to the Lorentz force, which depends on their momentum. Electrons that did not undergo bremsstrahlung are directed into the beam dump, where they are stopped. Bremsstrahlung electrons are deflected more due their lower momentum and hit the Tagger hodoscope, which is segmented into 120 channels and covers the electron energies 10% to 90% of the beam energy. Taking the Lorenz force into account, it is possible to determine the energy of the electrons by measuring which hodoscope detector was struck. The corresponding bremsstrahlung photon than has the energy E_γ calculated from the energy difference of the beam energy E_e and detected electron energy E'_e [5].

$$E_e - E'_e = E_\gamma \tag{2.1}$$

The flux of the photon beam is monitored with the GIM and Flumo detectors at the end of the experiment.

ARGUS

To increase the energy resolution the ARGUS detector was constructed, which now complements the Tagger hodoscope. ARGUS uses scintillator fibres to detect electrons. Each fibre covers a smaller region than one segment of the Tagger, which leads to a more precise position resolution and thus energy resolution [6, 7].

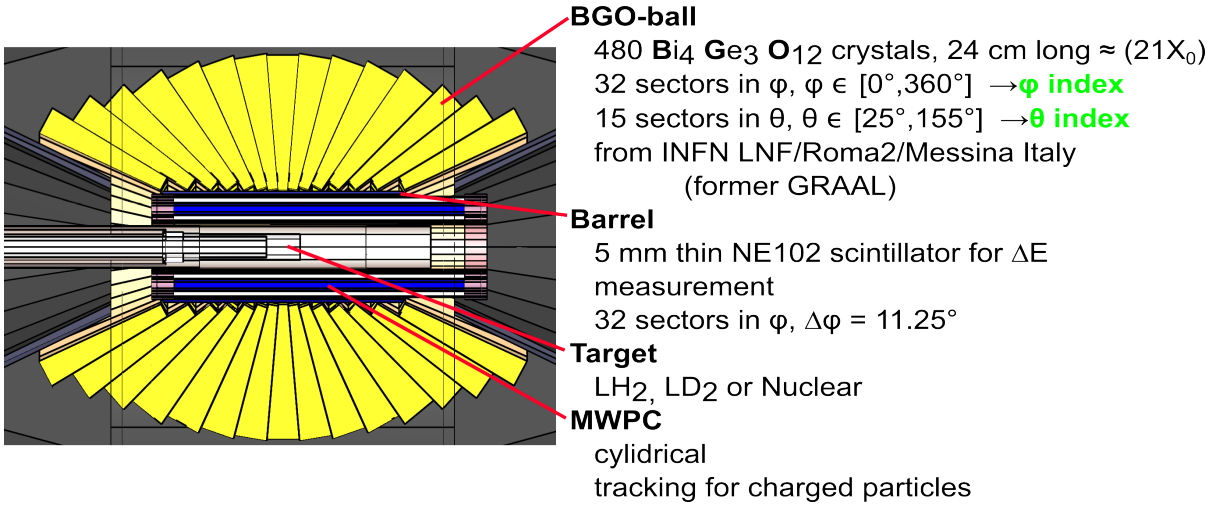

Figure 2.3: Slice view of the BGO ball.

2.2.2 Central Detector

The photons travel along a beam pipe and impinge the target, which is at the centre of the BGO ball. A slice view of the BGO ball is shown in figure 2.3. The target cell can be filled with liquid hydrogen or deuterium. Alternatively, a nuclear target can be used instead. Surrounding the target is a cylindrical multiwire proportional chamber (MWPC). This gas detector is used to reconstruct tracks of charged particles [8].

Scintillator Barrel

Around the MWPC, 32 thin plastic scintillator bars of thickness 5 mm are arranged in the form of a cylindrical barrel. This detector is used to identify charged particles and measure energy deposition. The energy deposited is only a fraction of the total energy and can be used together with the total deposited energy in the BGO calorimeter for particle identification.

BGO calorimeter

The BGO calorimeter consisting out of 480 bismuth germanium oxide (BGO) crystals is used to measure the kinetic energy and direction of particles. It was originally used in the GRAAL experiment. The BGO calorimeter covers with 15 sectors in θ, the angles from 25° to 155°. Each crystal is 24 cm long which correspond to approximately 21 X_0 radiation lengths covering $\Delta\phi = 11.25°$ for azimuth and $\Delta\theta = (6..10)°$ for polar angle. The advantage of bismuth germanate as a scintillator is the good energy resolution and a small radiation length. With the BGO ball it is possible to measure the energy of charged particles and photons. The light readout is done via photomultiplier tubes (PMT).

2.2.3 Intermediate Detector

Particles moving in forward direction with θ lower than 25° are outside of the central detector acceptance. In the θ region of 10° to 25° charged particles should be detected by the intermediate detector Daisy and SciRi. Both detectors are placed between MOMO and the BGO calorimeter.

SciRi

To cover this region the Scintillating Ring (SciRi) was build to close the acceptance hole of 10°-25° and is the subject of this thesis. Further details can be found in chapter 4.

Daisy

The Daisy detector consists of multigap resistive plate chambers (MRPC). This detector was under construction during the course of this thesis, it will cover the θ angles from 8° to 25° [9]. The advantage of this detector is the high detection efficiency and a time resolution of approximately 50 ps, which will allow for time-of-flight measurements.

2.2.4 Forward Spectrometer

If the θ angle of a charged particle is smaller than 10° the momentum and time of flight can be measured with the forward spectrometer. The open dipole magnet is used to deflect charged particles with its magnetic field. Tracking detectors before and after the magnet measure the particle direction from which the momentum than can be calculated. At the end three scintillator walls (ToF) are used to measure the time of flight which is used for particle identification [10–13].

MOMO and SciFi2

MOMO and SciFi2 are both scintillating fibre detectors which are used to measure the particle direction before the magnet. The readout of the light is done via PMTs which have a strong shielding against magnetic fields [10].

Open Dipole Magnet

The open dipole magnet used in the BGO-OD experiment is on permanent loan from DESY. It can produce a magnetic field up to 0.4 T and also has a fringe field in the close proximity. This fringe field, unfortunately, negatively impacts PMTs by reducing the overall gain [11].

Drift chambers

The particle direction after the magnet is measured with 8 drift chambers. These chambers have parallel wires inside. Two chambers are rotated by 90° to allow the measurement of the vertical and horizontal direction. Additionally, four of the chambers are rotated by 9° [12].

ToF

To measure the time of flight, three walls with horizontal plastic scintillator bars are used. This bars are readout with a PMT on each side. This allows for the calculation of the horizontal hit position of the particle from the time difference between the two PMTs, which are at either end of the scintillator. The vertical position is given by the bar itself. The time information from the Tagger is used as a start for the time of flight calculation [13].

CHAPTER 3

Sample reactions

In this chapter the importance of covering the θ acceptance gap from 10° to 25° by using several sample reactions will be illustrated. To simulate the kinematics, the ExPlORA framework together with the event generator is used. The event generator software calculates the kinematics using the known cross section and the characteristic $1/E_\gamma$ falloff for the bremsstrahlung process. The ExPlORA [14] framework is based on ROOT [15] and is used for this work in analysing both simulated and real data. In simulations Geant4[16] is used for particles passing through matter. In table 3.1 the selected reactions, which were investigated during this thesis, are shown. When a meson decays through the strong or through the electromagnetic mechanism, it is too short lived to measure directly. The daughter particles must be identified to reconstruct the parent meson. For example the π^0 meson decays 99% of the time almost immediately into two photons. The charged π, on the other hand, has a long enough life time to be detected in the detector. The η meson has many final states similar to the ω and η'. Similar to π^0 it can also decay into two photons, which is used in the η' reconstruction. The η meson was already observed by the BGO-OD detector in his two and six photon decay, thus it was used for testing the reconstruction algorithm.

Meson	Decay channel	Branching Ratio / %	Mass / MeV
η	$3\pi^0 \rightarrow 6\gamma$	31.6	547.85 ± 0.02
η	$\pi^+ + \pi^- + \pi^0 \rightarrow \pi^+ + \pi^- + 2\gamma$	22.5	547.85 ± 0.02
ω	$\pi^+ + \pi^- + \pi^0 \rightarrow \pi^+ + \pi^- + 2\gamma$	88.3	782.70 ± 0.12
η'	$\pi^+ + \pi^- + \eta \rightarrow \pi^+ + \pi^- + 2\gamma$	16.9	957.78 ± 0.06
η'	$2\pi^0 + \eta \rightarrow 6\gamma$	8.2	957.78 ± 0.06

Table 3.1: Selected mesons decay channels. [17]

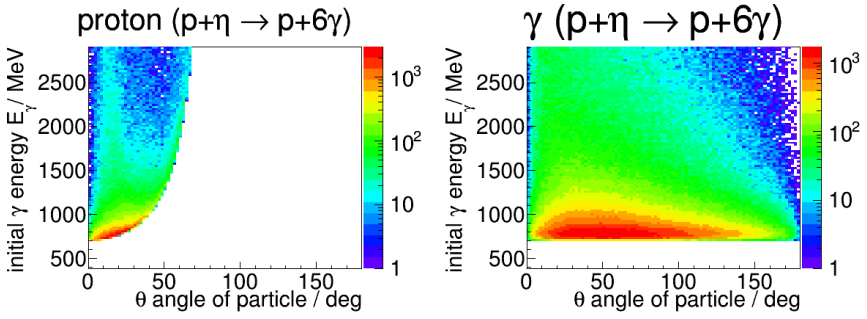

Figure 3.1: $\gamma + p \rightarrow p + \eta \rightarrow p + 6\gamma$ reaction. Initial photon energy E_γ against θ angle of particle. Left: proton. Right: γ

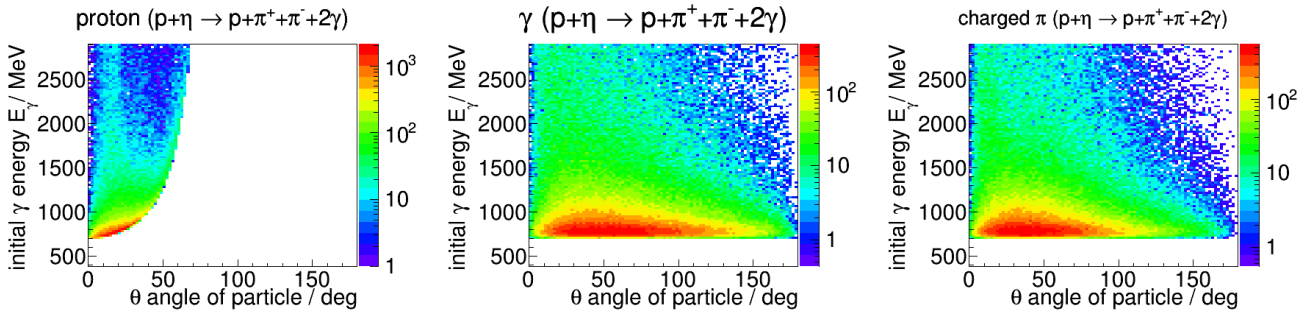

Figure 3.2: $\gamma + p \rightarrow p + \eta \rightarrow p + \pi^+ + \pi^- + 2\gamma$ reaction. Initial photon energy E_γ against θ angle of particle. Left: proton. Middle: Charged π . Right: γ

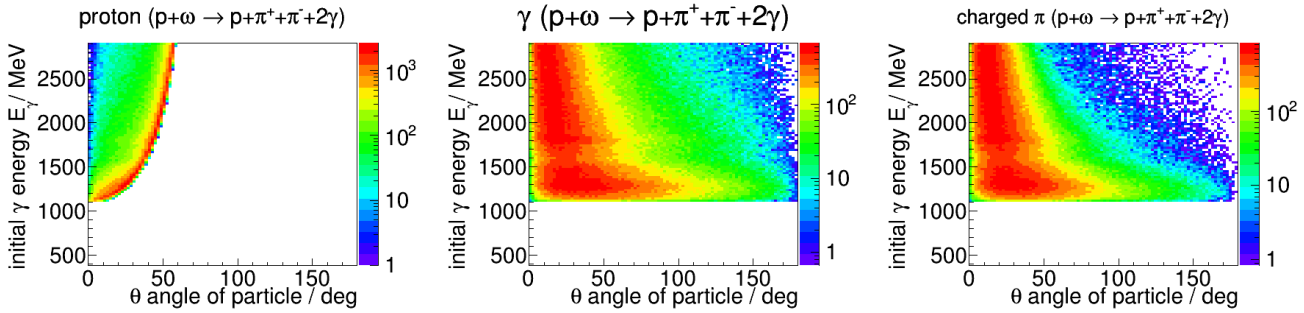

Figure 3.3: $\gamma + p \rightarrow p + \omega \rightarrow p + \pi^+ + \pi^- + 2\gamma$ reaction. Initial photon energy E_γ against θ angle of particle. Left: proton. Middle: Charged π . Right: γ

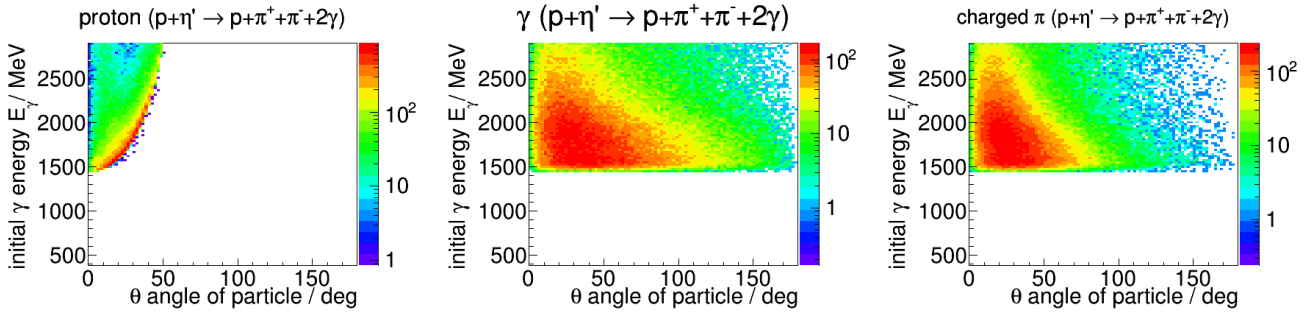

Figure 3.4: $\gamma + p \rightarrow p + \eta' \rightarrow p + \pi^+ + \pi^- + 2\gamma$ reaction. Initial photon energy E_γ against θ angle of particle. Left: proton. Middle: Charged π . Right: γ

3.1 Kinematics

It is important to understand the kinematics of a reaction and know the direction and energy distribution of the particles that may be detected. This can also be used to estimate the detector acceptance for the meson decay particles and the recoil proton direction. In the following plots the initial photon energy E_γ is plotted against the θ angle of the particle in the title. Using the physics-based event generator, the frequency distribution of each particle is filled into the histograms. In figure 3.1 the kinematics for the $p + \eta \rightarrow p + 3\pi^0$ reaction is shown. Comparing to the reaction $p + \eta \rightarrow p + \pi^+ + \pi^- + \pi^0$ in figure 3.2, one can see that the distribution of the photons and protons are almost the same. All particles preferentially travel in forward direction, which is normal for a fixed target experiment like BGO-OD due to the Lorentz boost.
In figure 3.3 the $p + \omega \rightarrow p + \pi^+ + \pi^- + \pi^0$ reaction is plotted. A similar picture is seen in figure 3.4 for the $p + \eta' \rightarrow p + \pi^+ + \pi^- + \pi^0$ reaction. Both the photons and charged πs can access the more backward regime in θ, but tend to be more forwardly directed. On the other hand, the kinematic reach of the protons limits the phase space acceptance in θ, which will never exceed 60°. In particular, in the photoproduction of ωs and η's, most protons will be very forwardly directed, i.e. $10° < \theta < 25°$, for photon energies between 1400 MeV and 2200 MeV. The kinematics for the $p + \eta' \rightarrow p + 3\pi^0$ reaction is similar to the $p + \eta' \rightarrow p + \pi^+ + \pi^- + \pi^0$ reaction and will not be discussed separately.

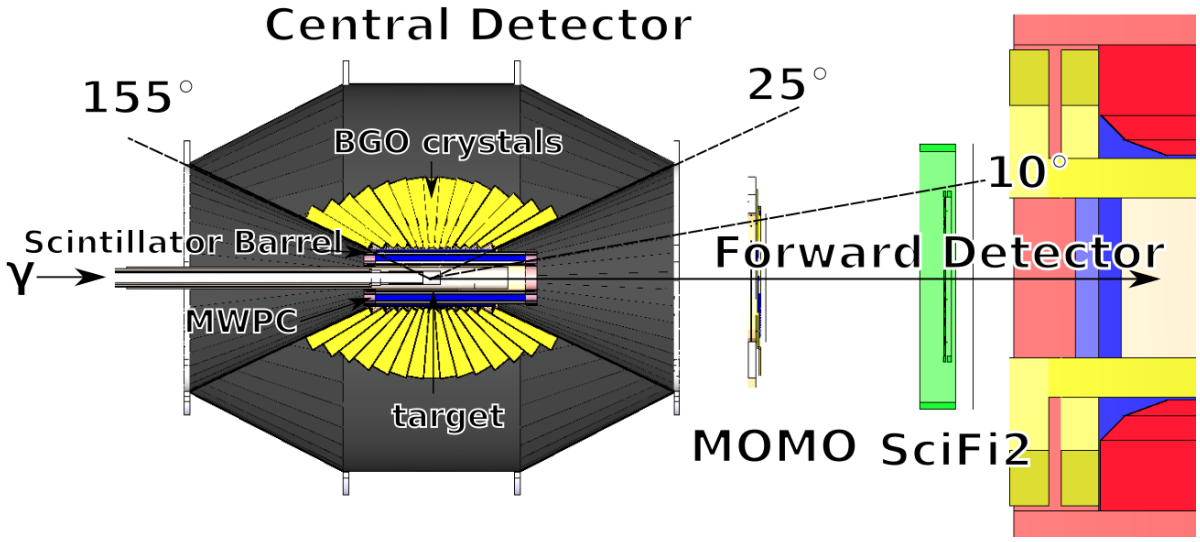

Figure 3.5: Slice view of the BGO ball and a part of the forward spectrometer.

3.2 Acceptances of the experiment

Knowing the general distribution of the particles is not enough to estimate reconstruction efficiencies. The BGO-OD detector does not possess full acceptance for the decay particles. The full BGO-OD detector is described in chapter 2. In figure 3.5 a slice view of the central detector and a part of the forward spectrometer are shown. The forward detector has an acceptance of up to 10° in θ for charged particles only. The BGO calorimeter can detect charged particles and neutral particles for θ angles 25° to 155°. When this thesis project began, an acceptance hole in the θ angle range of 10° to 25° was

present. There was no detector covering this. This is precisely the region where the final state protons would preferentially go in the photoproduction of ωs, ηs and η's.
The acceptance gap for $\theta > 155°$ is unimportant as very few final-state particles travel in the backward kinematic region.

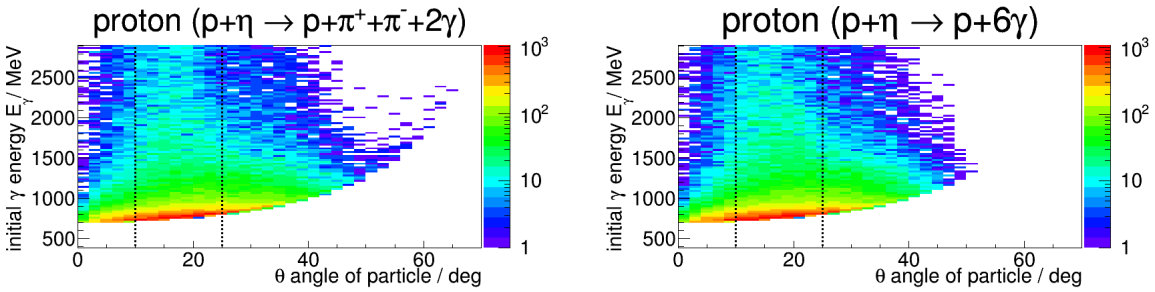

Figure 3.6: Initial photon energy E_γ against θ angle of proton. Decay particles of the meson within detector acceptance. Left: $p + \eta \to p + \pi^+ + \pi^- + 2\gamma$ reaction. Right:$p + \eta \to p + 6\gamma$ reaction

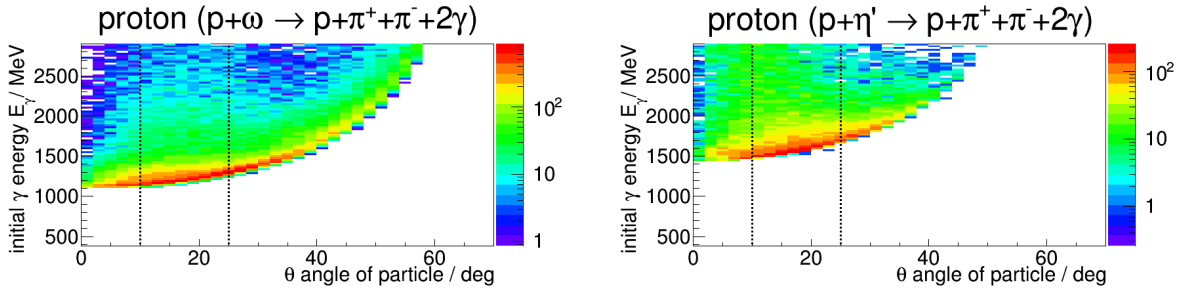

(a) $p + \omega \to p + \pi^+ + \pi^- + 2\gamma$ reaction.

(b) $p + \eta' \to p + \pi^+ + \pi^- + 2\gamma$ reaction

Figure 3.7: Initial photon energy E_γ against θ angle of proton. Decay particles of the meson within detector acceptance.

3.3 Proton angular acceptance

The polar angular distributions for the final-state proton were investigated by taking the angular acceptances of the detectors into account. Using the aforementioned acceptances in section 3.2, all events are ignored where the final-state particles cannot be fully detected. Charged π with a θ of 25° to 155° or $\theta < 10°$ can be detected by the BGO-OD detector. Photons can only be detected in the BGO calorimeter in the θ region 25° to 155°. By looking in the kinematics in figures 3.1, 3.2, 3.3 and 3.4 one sees that a part of the charged π and photons cannot be detected due to the acceptance hole in the θ angle range of 10° to 25°. Now all events are ignored where one of the photons or charged π may not be detected due to the detector acceptance. The only thing not constrained is the proton direction, which will be analysed for η, η' and ω separately. Shown in figure 3.6 is the proton θ distribution for the η reactions and in figure 3.7 for ω and η'. Now the protons are distributed between the θ angles 5° and 40° almost independent of the meson. Lacking a detector in this 10° to 25° θ regime, therefore, would jeopardize the experiment. It is absolutely imperative to close this acceptance gap.

The construction of the MRPC(Daisy) would not be ready for our first three-week production run. It was therefore decided to build another detector to close this acceptance hole. A stopgap measure was urgently needed. Less than six months to design, construct, test, calibrate and implement such a detector were available. Such is the genesis of the SciRi detector.
Given the highly abbreviated timeline, it was decided that the stopgap detector need only provide rather coarse solid angle information of charged particles trajectory in the $10^\circ < \theta < 25^\circ$ θ regime. In the following chapters, the construction, test and use in meson reconstruction of the SciRi detector will be discussed.

CHAPTER 4

Scintillating ring detector (SciRi)

The **Sci**ntillating **Ri**ng detector (SciRi) is a segmented plastic scintillator detector with Avalanche Photodiode (APD) readout. It was designed to cover the θ angles between 10 and 25 degrees. The detector is segmented into 96 pieces with each piece covering $\Delta\phi = 11.25°$ and $\Delta\theta = 5°$. A plastic scintillator is used to produce light, which is converted into an electrical signal after entering an Avalanche Photodiode. This analog signal is preamplified, shaped and finally discriminated into a logical signal. In the end, the signal is acquired with a time to digital converter (TDC).
The build detector was tested by using the $\gamma + p \rightarrow \pi^0 + p$ reconstruction at the end of this chapter.

4.1 Requirements

As for every detector, the SciRi detector had strict requirements to fulfill. The detector needed to be ready within a tight time schedule. This of course influences how complex the detector can be constructed, as a more complex design could consume too much time for the construction phase and thereby jeopardize the completion before the deadline.

Time Schedule

The planning for the SciRi detector started at the beginning of 2015. SciRi is a temporary solution to the still as yet not ready Daisy detector (Section 2.2.3), which will be fully operational by the end of 2015. It was planned for the Daisy to replace SciRi due to improved time and position resolution. Using SciRi additional to the Daisy would lead to multiple scattering for particles moving through SciRi into the Daisy, and so to have accurate Daisy data the SciRi detector needs to be removed. As such the SciRi detector needed to be fully operational before the June beamtime to maximise the period of operation. It is still under investigation if the SciRi detector could contrary to the previous statement complement the Daisy detector. To have a clear answer to this, both detectors needs to be operational. During the course of this thesis the fully operational SciRi detector was build into the BGO-OD experiment before the June beamtime.

Resolution requirements

Position: The position resolution should be comparable to the resolution in the BGO calorimeter. 32 segments in phi and 3 segments in θ were proposed. This leads to a total of 96 channels with $\Delta\phi = 11.25°$ and $\Delta\theta = 5°$.

Time: No time resolution requirement was set. Provided the signal can be associated to the time of the Tagger.

4.2 Construction

The SciRi detector was designed to the requirements mention in section 4.1. Following some design aspects like location of the detector, particle detection and read out are approached.

4.2.1 Detector material and particle detection

A plastic scintillator was used for particle detection. To complete the detector before the deadline no new scintillator material could be ordered and so old pieces of scintillator were used. This material was used to cut the scintillator pieces for SciRi. With this the SciRi detector got its scintillator almost for free. The disadvantage of the scintillator material is that the exact composition is not known. Also as it was previously used in experiments, some radiation damage was to be expected.

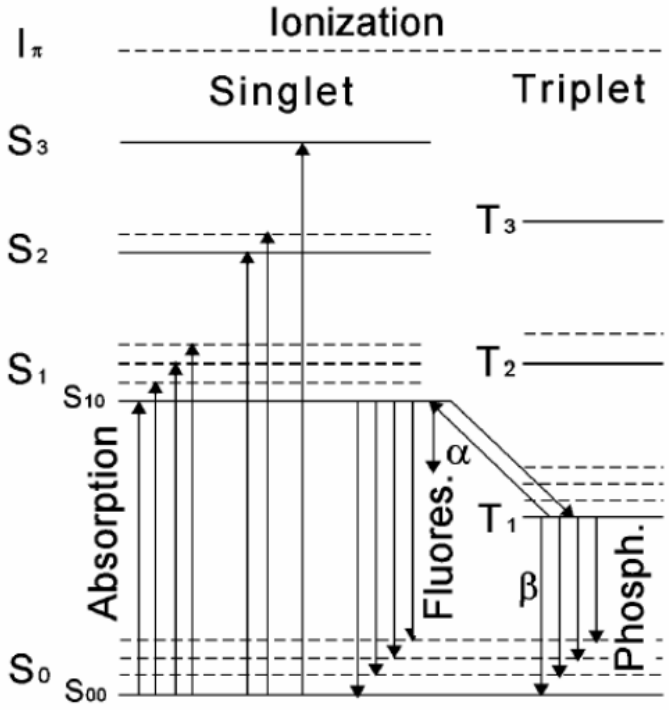

Figure 4.1: Energy levels of organic scintillating molecules.[18]

Organic scintillator

Organic scintillation arises from transitions in energy level structure of the molecule. An example for this can be seen in figure 4.1. The ground level for the electrons is the S_{00} state. The excitation of this state are S_1, S_2, S_3 ... . Each of these have a fine splitting due to different vibration modes. Similar to that the spin=1 states exists, which are represented by a T.
Through excitation with ionising radiation, the electrons transit to a higher level from the ground level S_0. The higher single states de-excite fast to the S_1 state without emitting radiation. States with excess vibrational energy like S_{11} or S_{12} lose this energy and move quickly to the S_{10} state. In the end almost all excitation from ionising radiation lead to the transition of the electron to the S_1 state.

The de-excitation of the S_1 for an organic scintillator is on the order of nanoseconds. As such the time resolution of this type of scintillator is really small. But the S_1 state can also transit to the T_1 state, where the de-excitation to the ground state needs more time but can be differentiated due to a different wavelength. The emitted photons are also not reabsorbed by the material as they possess less energy than needed. With the exception of the $S_{10} \rightarrow S_{00}$ transition, all other transitions emit photons with less energy by converting remainder of the energy into vibrational modes. These vibration modes lose their energy quickly and move to the S_{00} where they cannot reabsorb the emitted photon. This is often referred as the Stokes shift. Further details on organic scintillating process can be found in [18–20].
Because organic scintillation only needs one molecule, it is possible to dissolve organic scintillator in a solvent, and polymerized into a plastic scintillator. This plastic scintillator is fairly cheap to produce and easily shaped into different forms. In addition to the organic scintillator, the plastic scintillator is also doped with a wavelength shifter. This component absorbs the scintillating light and remits a light with a longer wavelength. This is important to shift UV light into the visible range as the polymer solvent is not UV transparent. Without it, the attenuation of light in the material would negatively affect the light gain.
To sum up, plastic scintillator are widely used in particle physics detectors as they are cheap, easily shapeable and have a good time resolution.

4.2.2 Arrangement and mounting

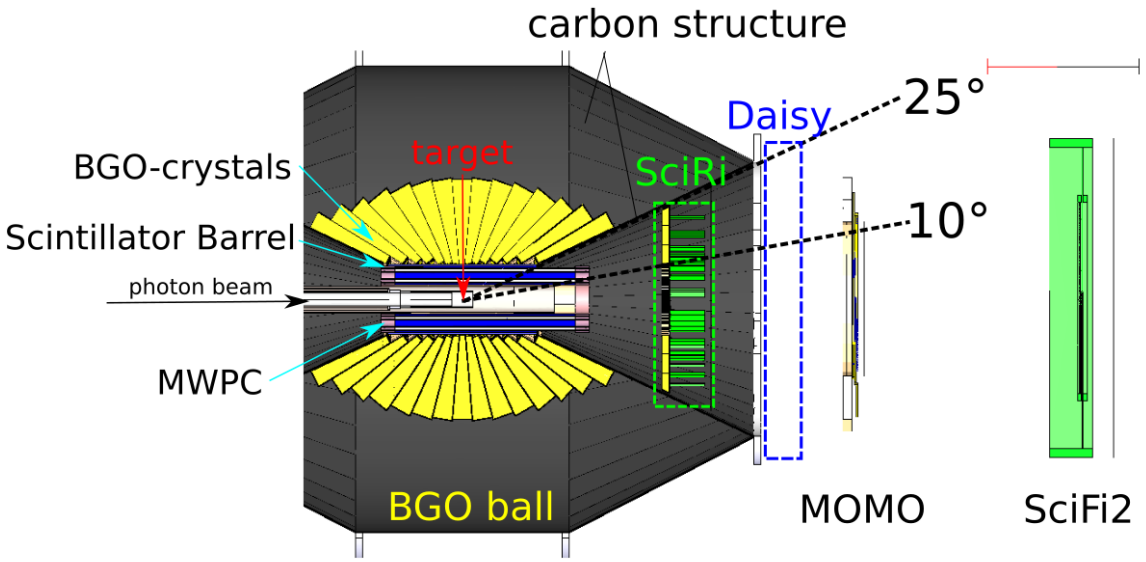

Figure 4.2: Overview of a part of the BGO-OD experiment. The photon beam enters from the left. This figure is taken from the ExPlORA simulation.

To cover the missing acceptance of the BGO-OD experiment, SciRi must be positioned between the BGO ball and MOMO. Due to limitations in space, SciRi is positioned inside the BGO-ball. In figure 4.2 the location of BGO ball, Daisy and SciRi can be seen. Going inside the BGO has the advantage that the detector dimensions are smaller and thus less material is needed for construction.
Building the detector inside the BGO has also disadvantages. First there is no holding structure on which

the detector can be mounted onto and secondly the dimensions of the carbon structure (see figure 4.2) where SciRi will be located are not known. The dimensions of the carbon structure could be determined with a precision of 5 mm. This was insufficient and could result in a gap between the carbon structure and SciRi. This region between the carbon structure and SciRi is really important as most protons land in here (see chapter 3). The solution was that the detector will be designed to be pushed as far as possible inside the BGO. This will close any gaps, as the carbon structure is cone shaped. If the outer dimensions of SciRi are bigger or smaller than the expected availible space, the detector will have a different distance to the target which will result in a change of acceptance. The expected angles can be corrected as soon the real detector location is known.
The SciRi detector has no mounting to the BGO structure. Because the period of operation for this detector will be less than one year, the detector will be taped to the carbon structure. The BGO ball can be opened by splitting into two halves, and so the SciRi detector also consists of two half rings. With this each half ring is taped to the corresponding BGO-halves. Each SciRi half weights around 3 kg, so tape was sufficient to hold the detector for a period of time. As tape is elastic and the glue partly fluid, it is advisable to check the position of the detector periodically.

Scintillator size

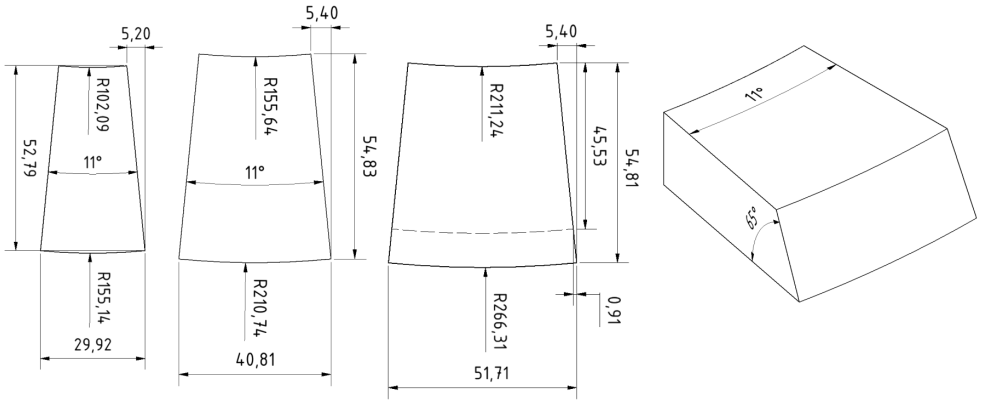

Figure 4.3: Measurement of the single scintillators which were used in the SciRi detector. The other ring has an angle cut to fit the scintillators better to the carbon structure and have a high efficiency in this region.

As mentioned in section 4.2.1, the SciRi detector uses plastic scintillator as the active material. This material is from an old unused detector which was then cut into the needed size by the workshop.
The scintillator bar had a thickness of 2 cm, which also applies to the scintillators in SciRi. In figure 4.3 the other dimensions of the scintillators can be seen. Each scintillator covers 5° in θ and 11.25° in ϕ. To account for production uncertainties and the needed space for the wrapping a 0.5 mm spacing between each scintillator was planned for. The full acceptance should be from 10° to 25° θ angle.

Scintillator mounting

To prevent the scintillation light from leaving the scintillator and create cross talk, they were wrapped in aluminium foil. The foil reflects UV and visible light, which is used to increase the number of photons reaching the APD through multiple reflections. The APD connection side on the scintillator is left without wrapping. This side is glued to an aluminium plate. With this the scintillators are fixed in place and the aluminium plate also reflects light on this side. The cutting for the plate is depicted in figure 4.4. For the APD window one needs to bend the small rectangular cuttings in the aluminium plate. These are also used to hold the electronic boards in place. On this plate an additional aluminium plate is mounted on it. The idea is to create a conductive box which shields the electronics inside from the electromagnetic fields (see section 4.2.3). The only side which has no conductive plate is on the side were the other detector half is located.

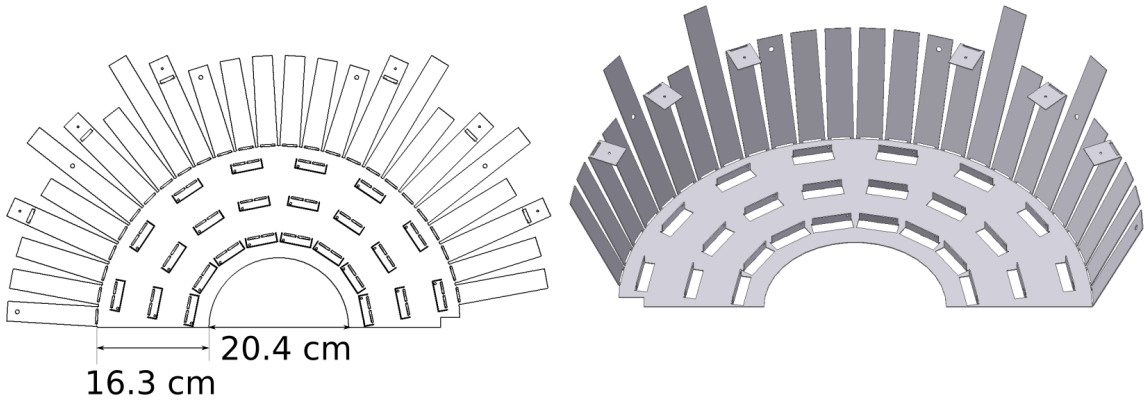

Figure 4.4: SciRi aluminium plate. Left: Unfolded plate. Right: Folded plate. The rectangular windows are for the APDs.

The glued scintillators and mounted APDs can be seen in figure 4.5. The black rectangular mark the sensitive area of the APDs. The transparent scintillators can be seen by the scintillator edges. Two APDs are connected on one small board (see section 4.2.3) with a fixed distance to each other. To use an APD per scintillator this board was placed at the gap between two scintillators. This makes the read out by the APD unsymmetrical in the scintillator. Due to the not 100 % reflective efficiency of the aluminium, the detection efficiency can be more position dependent compared to the symmetric case. To reduce this effect, the SciRi detector was placed as near as possible to the target. The minimum distance to the target for the detector was determined by the inner scintillator ring. One can see in figure 4.5 the scintillator is almost as wide as one APD. The position of the SciRi detector was therefore determined by this.

Detector model

In figure 4.6, one SciRi half inside the BGO carbon structure is shown. The green pieces inside the SciRi mark the electronics. The yellow lines show the 10° and 25° θ angle at the cut plane. The photograph of the build-in detector can be seen in figure 4.7. The interior of the detector is protected against light by a black foil.

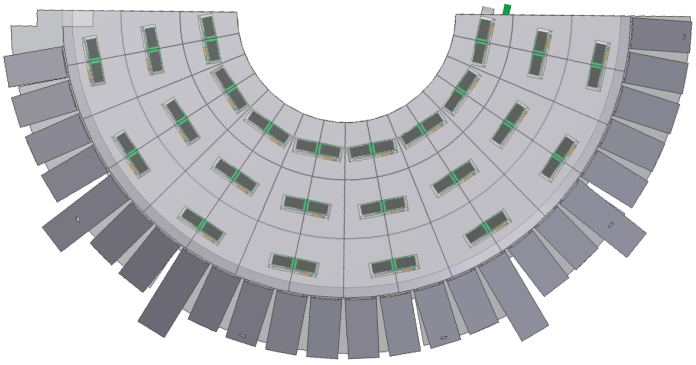

Figure 4.5: Front view of the SciRi detector. Scintillator are transparent but the edges are visible. The solid black rectangles are the APDs.

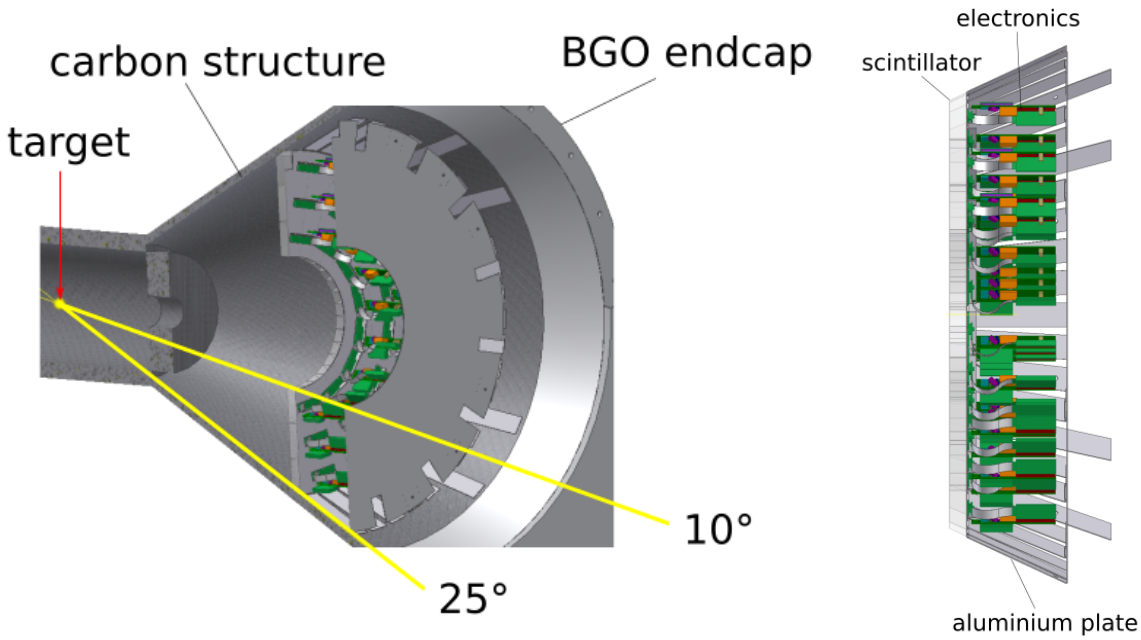

Figure 4.6: Right: SciRi model inside the BGO carbon structure. Left:Side view of the SciRi detector with electronics.

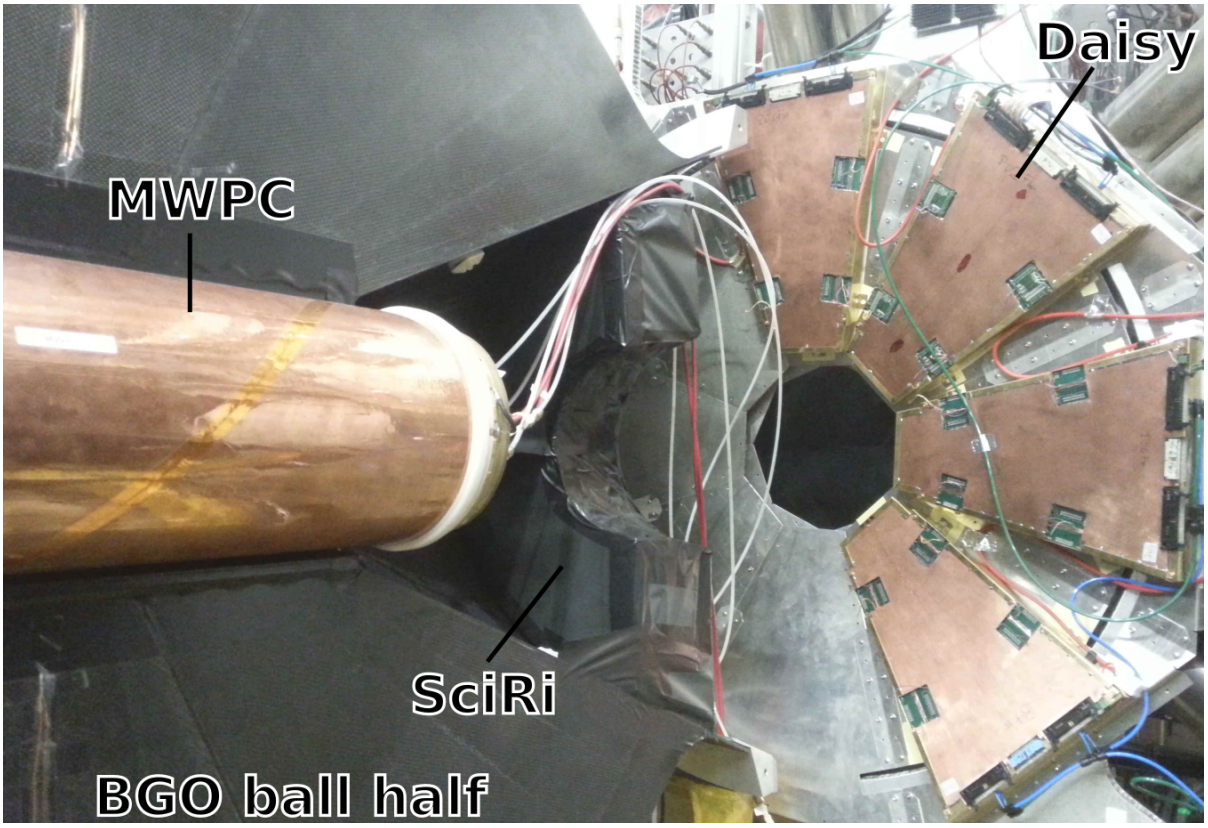

Figure 4.7: Photograph of one SciRi half build in the experiment. In this photograph, the BGO ball was opened for maintenance.

4.2.3 Electronics

A chain of electronics is necessary to get an electric signal from the scintillation light. This starts with an Avalanche Photodiode which creates a small pulse from the incoming light. This signal is preamplified and shaped before it can be discriminated. With this now logical signal, time information can be obtained using a time to digital converter (TDC). The opened detector with part of the electronics can be seen in figure 4.15.

Avalanche Photodiode

The Avalanche Photodiode (APD) is a special variation of the photodiode. This kind of photodiode acts similar to a solar cell. Through excitation in the depleted region, an electron-hole pair is produced. Due to the electric field, the electron and hole drift apart. When recombining through the circuit a measurable current is produced. This Photodiode would have no gain as there is no amplification of the electron-hole-pairs. It is expected that one charged particle would produce photons in the order of 10^3 inside the scintillator. Without any further amplification, this small signal cannot be differentiated from electronic noise.
An Avalanche Photodiode has an additional layer in which the electrical field is really strong. This can be seen in figure 4.8. This layer is achieved by a strong doping of the silicon. Here the depleted

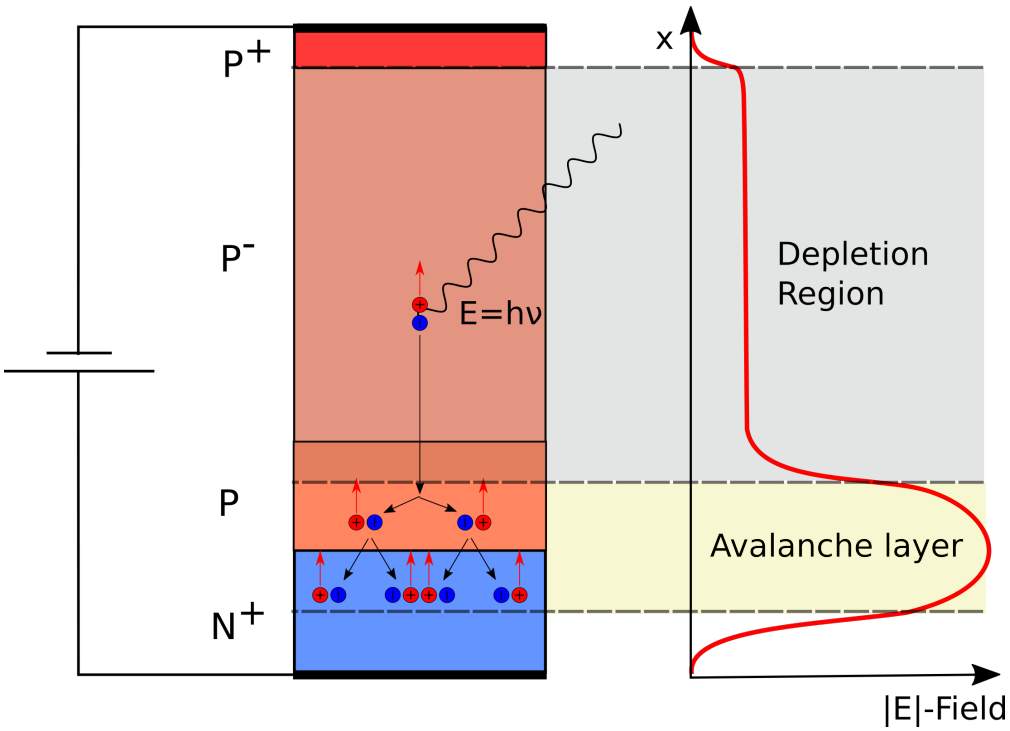

Figure 4.8: Principle of Avalanche Photodiode operation.

region is marked by a grey area and the Avalanche layer by an yellow layer. The electrons gain enough momentum to create additional electron-hole pairs in this amplification layer. This amplification of the initial electron-hole pair is in the order of hundreds. The gain can also be increased by applying a higher voltage on the APD. This is at maximum when the break down voltage is reached. In this region the thermal exaction is enough to produce an electron-hole-pair. Which leads to a continuously avalanche discharge until the diode breaks down due to the high current. With this the APD acts similar to a gas detector [20]. An example of an APD used in our experiment can be seen in figure 4.9.

The advantage of APDs over photomultiplier tubes is that they are insensitive to magnetic fields. This

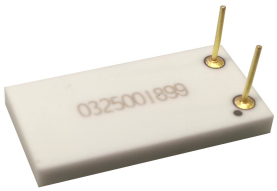

Figure 4.9: Avalanche Photodiode used in the SciRi detector. Hamamatsu S11048(X3) APD.[21, 22]

helps because some fringe field from the Open Dipole magnet is still measurable in the SciRi position. As the APD only produces small signals, a high pre-amplification is needed. The electromagnetic fields can be picked up by the electronic and amplified. To reduce this pick up a Faraday cage is needed which is depicted in section 4.2.2. Additionally, it is expected that the sensitivity is lower compared to a photomultiplier tubes.

Preamplifier

The APDs (figure 4.9), preamplifier (figure 4.10) and HV boards (figure 4.12) for the SciRi detector were given to the BGO-OD experiment from the Crystal Barrel experiment (CBTAPS) [21, 23, 24]. These were spare parts for the Crystal Barrel calorimeter [21–23], where two APDs per crystal are used. This also reflects in the preamplifier design. It contains two preamplifier circuits per board and two connections to APDs. On each side of the board a preamplifier circuit is present, but the layout of the electronics on the board is different for both circuits. Also the preamplifier was constructed for CsI(Tl)-crystal scintillators. This inorganic scintillator produces light on a longer time scale than the plastic scintillator from SciRi. Also one expects high energy deposition in a calorimeter of the order 10^2 MeV, which is different in a 2 cm thick plastic scintillator, where one expects energy deposition in the order of few MeV.

This results in setting the gain of the APD higher than for the Crystal barrel setup. The maximal set

Figure 4.10: Preamplifier for the APD. Two APDs can be mounted on the right small board. This board is connected through a 7 cm bus with the preamplifier board. The blue cables are connected to the Negative Temperature Coefficient Thermistors (NTC), which allows a temperature measurement.[25]

gain is different for each APD, ranging from a factor 300 to 1000. This comes from the fact that the APDs were not constructed for this gain range and fabrication differences determine the maximal gain. The width of the preamplified signal was bigger than a microsecond. This exceeded the time window of the TDC so shaping was needed to measure the time over threshold. The shaping of the signal is done on the SciRi Mainboard by using a capacitor in series. This is the simplest shaping method and has the disadvantage of lowering the pulse amplitude significantly. It turns out that at gain 200 only small signals of around 6 mV for minimum ionising particle are produced after shaping, which is to low to be effectively discriminated from noise. To solve this problem, the preamplifier was modified. Some of the electronic components can be seen in figure 4.11. Capacitors marked with a red cross were removed for the SciRi detector. The 220 pF and 150 pF were specifically chosen for the Crystal Barrel crystals. The light output of the plastic scintillator is faster than these crystals, so these capacitors were removed to decrease the rise time of the signal. The capacitor C1 was planned to be changed from 6.8 pF to 0.47 pF capacitance to gain a factor 14 in the amplification. As this is a really small value it was removed instead. The remaining open contact should produce a capacity of similar magnitude. This also reduces the falloff time of the signal which should decrease the deadtime of the detector. The exponential falloff constant, τ, can be estimated with $\tau = R \cdot C$ [23, 25].

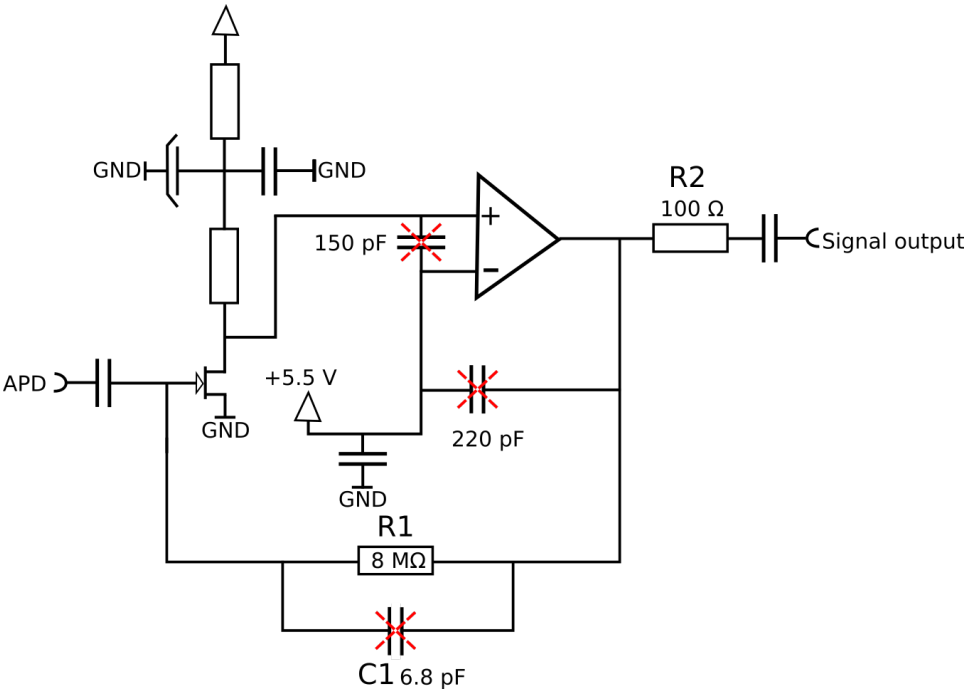

Figure 4.11: Components of the preamplifier. The red crossed capacitors were removed.[23, 25]

HV Board

The high voltage board (HV board) is used to set the high voltage, which is applied to the APD. It can be seen in figure 4.12. Every HV board supplies two APDs with a high voltage. By setting a potentiometer on the board, a constant 500 V is scaled down to the needed APD voltage. Additionally the APD temperature and the output voltage can be readout using analog-digital converter (ADC).

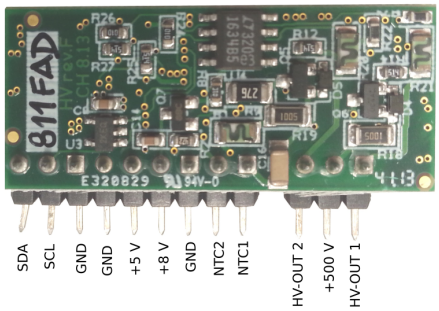

Figure 4.12: High voltage board (HV Board). This board supplies two APDs with high voltage. [25]

SciRi Mainboard

The HV board needs to be connected to the Preamplifier. Also a means of communication needs to be established. For this reason the SciRi Mainboard was designed by Thomas Zimmermann [26]. The

HV-Board and Preamplifier can be attached to it. In figure 4.13 a photograph of the SciRi Mainboard is shown. The upper connection on this board is used for a bus. This bus supplies the board with the needed -2 V, +5 V, +8 V and +500 V. Additionally one can communicate with the microcontroller which is seen on the left side of the board. On the lower left side one can attach the HV-Board and on the lower right side the Preamplifier.

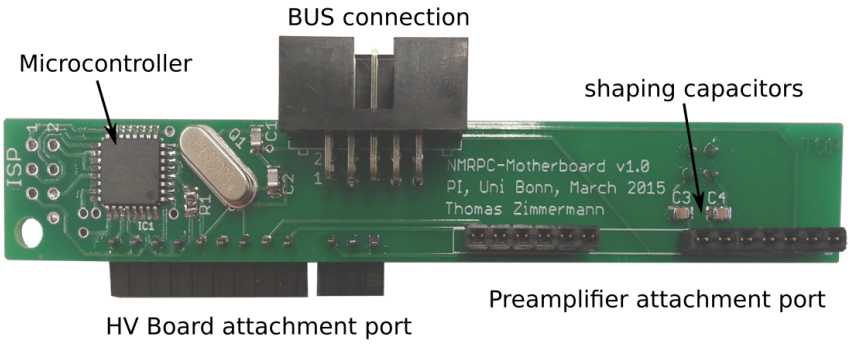

Figure 4.13: SciRi Mainboard. This board connects the HV board and Preamplifier to the bus. It also has a microchip to communicate with the HV board. One can read NMRPC-Motherboard written on the board. This was the name of SciRi detector during planning.

The Preamplifier output signals are shaped using a capacitor connected in series. In this case the capacitor has the role of a low-frequency filter, resulting in a discriminated signal from the original output. A sketch of the signal before and after the shaping can be seen in figure 4.14. With smaller capacitance, the signal width will be more narrow. This type of shaping comes with a price of a smaller amplitude than the original signal. This is countered by modification of the Preamplifier which is described in section 4.10. In the end a 330 pF capacitor was used for shaping.
To set the high voltage on the HV-Board a responsible potentiometer needs to be set. To set it, a microcontroller is present on the SciRi Mainboard, which in return can be controlled via bus connection.

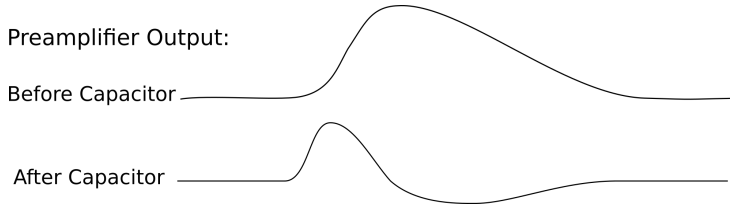

Figure 4.14: Sketch of an output signal before and after capacitor in series.

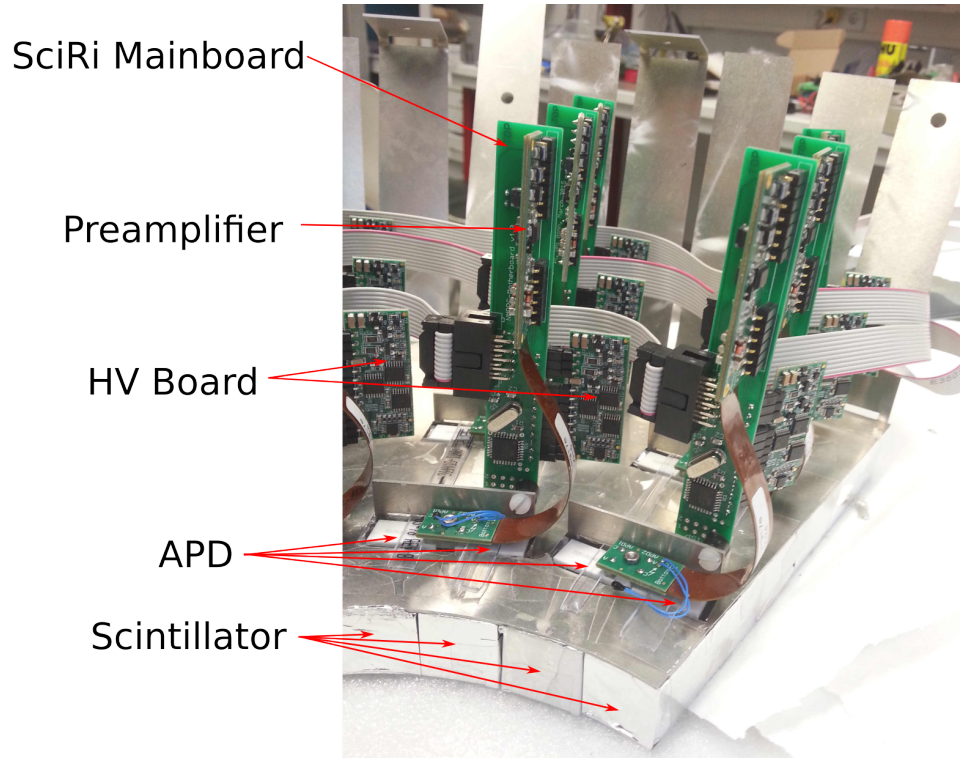

Figure 4.15: Opened SciRi detector. One quarter of the SciRi half is seen in the photograph.

SciRi Voltage Supply Board

The SciRi Voltage Supply Board which is shown in figure 4.16 produces different voltages needed for the SciRi Mainboard. This board was also designed by Thomas Zimmermann and converts a 12 V DC voltage into -2 V, +5 V, +8 V and +500 V. One board is connected via bus to 8 SciRi Mainboards. The +500 V module can produce enough current to supply 24 boards. To lower the cost 3 SciRi Voltage Supply Boards are connected. A IC is build in to communicate via USB with the bus, which is used for the SciRi Mainboard microcontroller communication. After plugging in the USB cable to a computer one can set the high voltage for the APDs. Some examples for commands are shown in table 4.1.

Command	Effect
T1P03R	Readout set potentiometer value of APD on θ-index 1 and ϕ-index 3
T2P04S0012	Set potentiometer to 12 of APD on θ-index 2 and ϕ-index 4
T3P04W415	Rename the index T3P04 to T4P15
T3P01A1	Read out ADC number 1. There are 4 ADCs.

Table 4.1: Possible Commands for the SciRi Board microcontroller.[26]

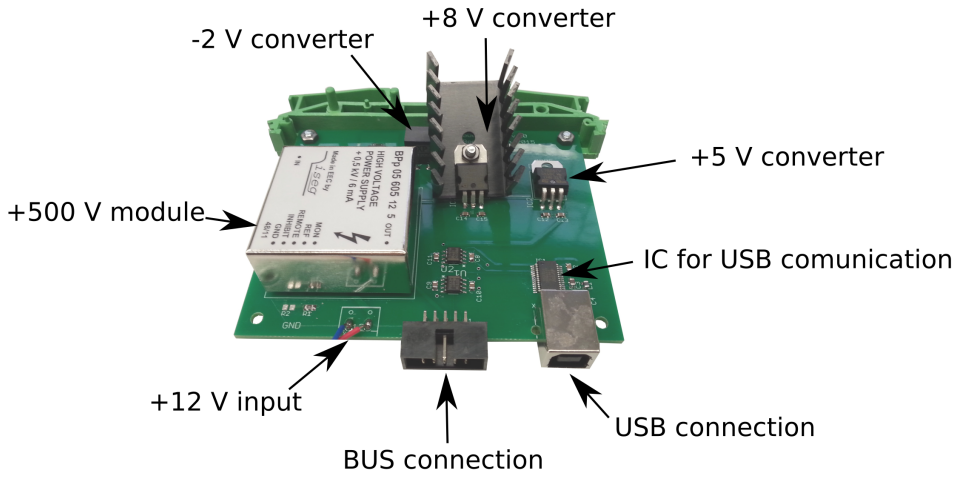

Figure 4.16: SciRi Voltage Supply Board. This board produces +5 V, +8 V, -2 V and +500 V out of +12 V. Additionally it has an USB interface.

Signal Readout

Figure 4.17: VFB6 FPGA board with 3 discriminator mezzanine attached.

The SciRi Mainboard amplifies and shapes the signals from the APD. This analogue signal needs to be discriminated into a logic signal before it can be applied to a Time-to-Digital Converter (TDC) to get time information. Also a logic is needed to form an OR signal of all channels which acts as a trigger signal for the BGO-OD data acquisition.

All these requirements are solved with an Field Programmable Gate Array (FPGA) board VFB6. Its a VME board designed by Elektroniklaboratorien Bonn (ELB) which utilises the Spartan 6 FPGA chip. Additionally one can plug-in up to 3 mezzanine boards with additional functions. In figure 4.17 the used board is depicted. In this case the mezzanine was selected to be a 16 channel time-over-threshold discriminator. This mezzanine discriminates the input signal and only produces a signal as long the input signal is over threshold. The width of the output signal is in that case the time-over-threshold (ToT). ToT can be used to correct the time-walk which occurs by different signal amplitudes and a normal threshold discriminator.

The FPGA is loaded with the jSciRi firmware. This firmware bases on the jTDCv6 firmware written by John Bieling [27]. The jTDC has a TDC implemented on the FPGA itself. To this basis a trigger logic specially for the SciRi detector was added. It can be set to produce a trigger on a cosmic event or just a simple OR of all channels.

4.3 Commissioning

One half of the SciRi detector was build in the BGO-OD setup during a one week test beamtime from 18th to 25th May. Because the results were positive, the full detector was operated during the data taking beamtime from 22nd June to 13th July. The following commissioning report refers to the data taking beam time.
It is assumed that mostly electrons are measured in the SciRi detector. These were primary used for testing and gain matching. As the energy deposited by elections should be smaller than by protons, it is ideal to use them for threshold setting and gain matching. The goal was to have maximum efficiency. As long one does not cut of the elections, due a to high threshold, one should expect to also see charged mesons,which are minimum ionising, and protons.

4.3.1 Time over threshold

As mentioned in section 4.2.3 additionally to the time information we get the time-over-threshold information. At the start of the beamtime the APD high voltage and the discriminator threshold were set to a point so that every channel has a comparable ToT distribution. The measured time-over-threshold distribution for every channel is plotted in figure 4.18. One can see that every second channel has a different mean point in the distribution. It also not possible to set the gain of all channels to a fixed ToT time. This is correlated to the APD connection on the preamplifier board. Even through the electronics used for both preamplifier circuit are the same, the location of these parts on the board are different. It could be that through the different connection locations a small capacitance is introduced, which affects the rise time of the preamplifier, and thus after shaping with a capacitor in series, the signal width. For the sake of gain matching the two preamplifier circuits were aligned separately. During the gain matching SciRi channel 47 was matched to the rest of the channels, but was apparently not correctly set at the end.

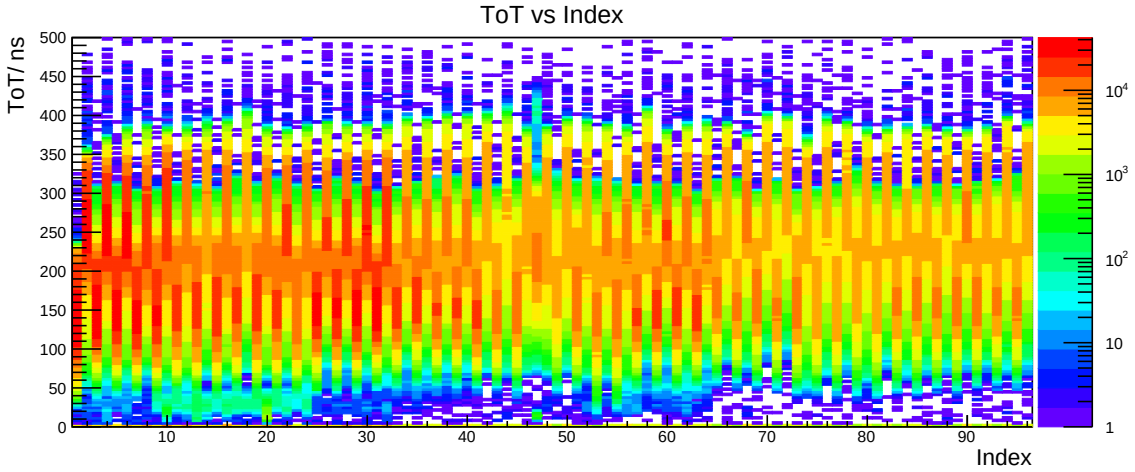

Figure 4.18: Time-over-threshold (ToT) versus SciRi channels (index) plot. Every second channel has a jump in the ToT mean point due to different signal forms.

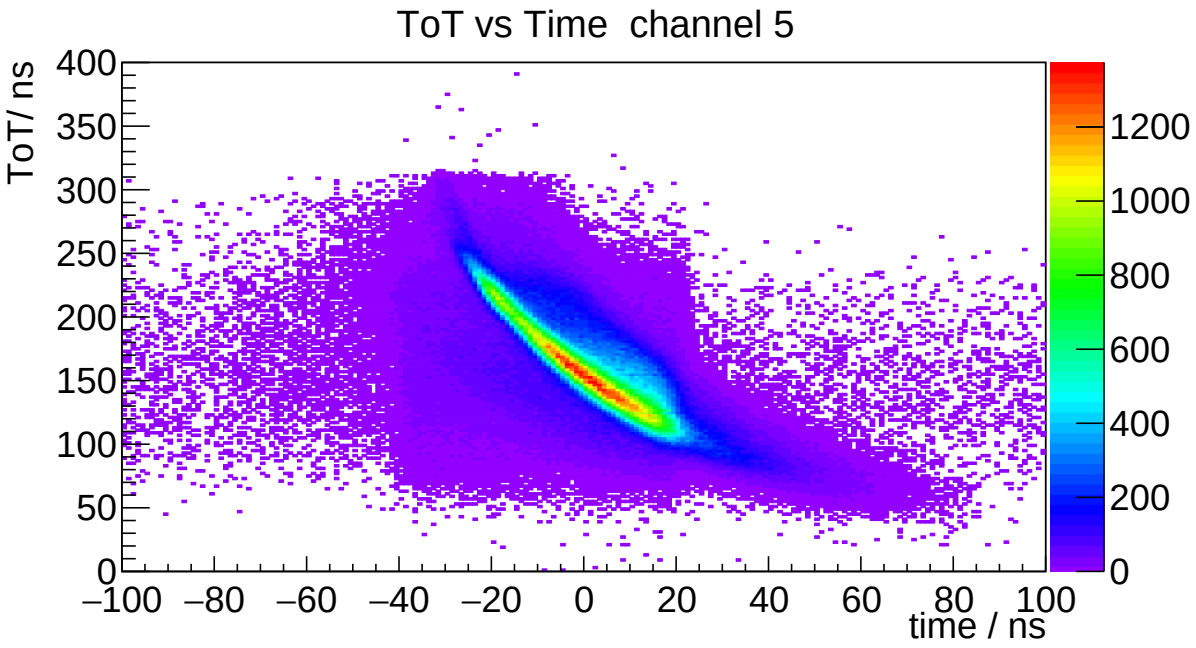

Figure 4.19: Time-over-threshold (ToT) versus time (index) plot. A clear time-walk can be seen.

4.3.2 Time-walk correction

As the discriminator is a constant threshold discriminator, a time-walk will occur which smears out the time resolution. The time-over-threshold (ToT) is plotted against time in figure 4.19 for one channel of SciRi. The time in the plot is the time difference to the event trigger. The experiment takes only data if a selected trigger condition is fulfilled. The time distribution of the SciRi detector has a good correlation to this trigger condition, and a low number of uncorrelated events. The relation between ToT and time was estimated as a 2nd order polynomial. For every channel the parameter of the polynomial was determine individually.

4.3.3 Time resolution

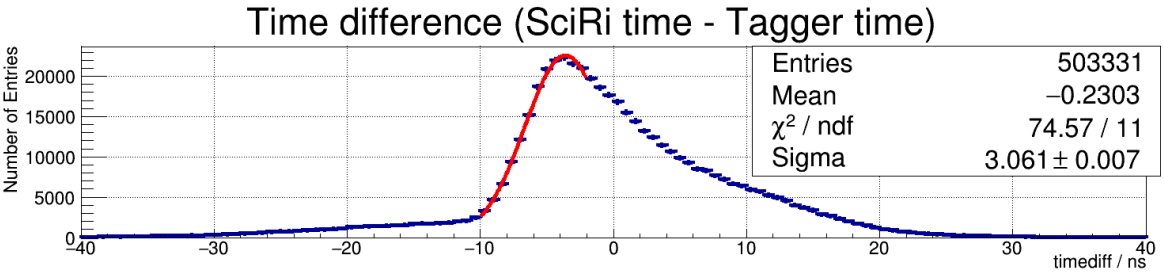

Figure 4.20: Time difference between SciRi and Tagger hits. A Gaussian was fitted to estimate the time resolution. The result is a σ of 3.06 ± 0.01 ns.

With the timewalk correction mentioned in section 4.3.2, one can try to determine the time resolution of the detector. To have a good estimate on the time resolution, the time difference between Tagger time and SciRi time was plotted in figure 4.20. The Tagger has a time resolution of around 200 ps, which can be neglected compared to SciRi time resolution.
Negative times correspond to events before and positive time after the hit in the Tagger. The right side of the distribution could be an artefact of the timewalk correction which for now is ignored during fit. From a fitted Gaussian one can conclude that the time resolution is in the order of 3.06 ± 0.01 ns. This time resolution, and the fact that the SciRi detector records low amount of noise, is sufficient to correlate hits in SciRi to hits in other detectors.
Constant time offsets which occur from the flight time of photons from Tagger to target are already subtracted. Remaining offsets stem from the timewalk correction. In plot 4.19 each slice of Y axis was fitted with a Gaussian function. The timewalk correction function then shifts the mean of the time distribution to zero. The real time distribution is not a Gaussian function, which leads to a time distribution with a peak at not zero.

4.3.4 Efficiency

The efficiency of the SciRi detector is limited by the geometry of the scintillators. Between each scintillator there is a gap of about 0.5 mm to provide room for scintillator cutting uncertainties and the aluminium foil to make the scintillator light tight. This leads to a dead space of about 1.5% in the acceptance area. This means that the detector has an expected efficiency lower than 98.5%.
To determine an efficiency it is necessary to know how many and which type of particles are hitting the SciRi detector. Normally one would put a detector before and after the SciRi detector and trigger on the coincidence of both detectors while checking the SciRi detector for a positive response. This was not possible in our case due to the required extra time to build such a setup. An indirect way to estimate the efficiency of the SciRi detector was performed. Through reconstruction of the $\gamma^0 p^0 \rightarrow p\pi^0$ reaction, the final proton can be used to determine the efficiency. For this π^0s were reconstructed using the BGO calorimeter. The π^0 decays into two photons, which can be detected with the BGO calorimeter. With a time correlated hit in Tagger one can calculate the initial state $\gamma^0 + p^0$. The Tagger hodoscope detects the bremsstrahlung electron with an energy information, which can be used to calculate the initial photon energy E_{γ^0}. The 4-momentum of the initial state $\boldsymbol{\gamma^0} + \boldsymbol{p^0}$ can be calculated with the assumption that the photon interacted with a proton, which can be assumed because a liquid hydrogen target was used. In equation (4.1) the initial state is calculated using the proton mass m_{p^0} and the tagged photon energy E_{γ^0}

$$\boldsymbol{\gamma^0} + \boldsymbol{p^0} = \begin{pmatrix} E_{\gamma^0} + m_{p^0} \\ 0 \\ 0 \\ E_{\gamma^0} \end{pmatrix} \tag{4.1}$$

By using the initial state and the reconstructed π^0 the proton's 4-momenta p can be calculated. If p has a θ angle between 10° and 25°, it is checked if the SciRi detector detected a particle in the same direction as the calculated proton. The efficiency is than the ratio between all events were the proton was found in SciRi and the total number of events. This way calculated efficiency is only the minimum possible efficiency, as there is no guarantee that the calculated proton reaches SciRi without undergoing strong scattering due to low momentum or if a $\gamma^0 + p^0 \rightarrow p + \pi^0$ reaction was actually present. What

we are calling efficiency is actually a convolution of detector acceptance, efficiency and reconstruction efficiency. It is used to check if the SciRi detector works as expected. An approach to determine the efficiency using cosmic radiation was performed by Paul Züge in his bachelor thesis [28].

π^0 reconstruction

As a starting point the π^0 is reconstructed. The π^0 decays into two photons, which can only be detected by the BGO calorimeter. These two photons should form two clusters from individual crystal hits. The clusters then contain the photon energy E_{γ^x} information and the position for photon x. By assuming that the photon originates from the target, the direction of the photon can be calculated from the position information. Events with only two clusters in the BGO calorimeter are selected. Further, we use the Scintillating Barrel to verify that the particle had no charge. The invariant 4-momentum $\boldsymbol{\gamma\gamma_{inv}}$ of the two photons is calculated with equation (4.2). The invariant mass $\gamma\gamma_{inv}^{mass}$ is then calculated using the angle $\theta_{1,2}$ between the photons directions in equation (4.3).

$$\boldsymbol{\gamma\gamma_{inv}} = \boldsymbol{\gamma^1} + \boldsymbol{\gamma^2} \tag{4.2}$$

$$\gamma\gamma_{inv}^{mass} = \sqrt{(E_{\gamma^1} + E_{\gamma^2})^2 - (\vec{p_{\gamma^1}} + \vec{p_{\gamma^2}})^2} = \sqrt{2 \cdot E_{\gamma^1} \cdot E_{\gamma^2}(1 - \cos(\theta_{1,2}))} \tag{4.3}$$

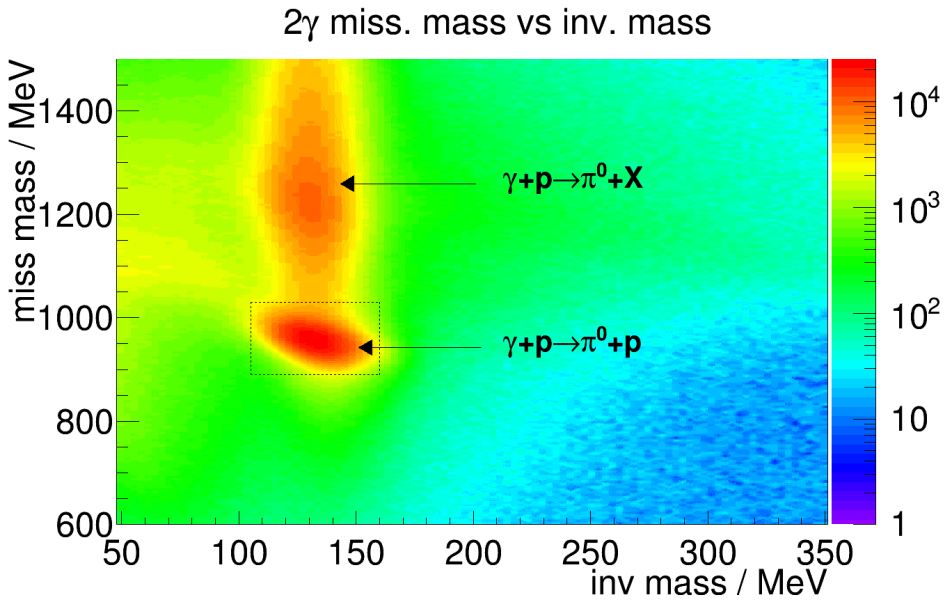

Figure 4.21: 2γ missing mass against invariant mass. The $\pi^0 + p$ peak is on top a background which mostly stems from the $\pi^0 + X$ reactions. X means all possible reaction with a π^0 in the final state except the $\pi 0 + p$ reaction.

Together with the initial state from equation (4.1) the missing 4-momentum $\boldsymbol{\gamma\gamma_{miss}}$ can be calculated with equation (4.5) and from this the missing mass $\gamma\gamma_{miss}^{mass}$ to the $\gamma\gamma_{inv}^{mass}$ in equation (4.7). The π^0 has a mass of around 135 MeV, while the proton has a mass of around 938 MeV [17]. In our reconstruction of the $\pi^0 + p$ events we expect that the invariant mass will give us the π^0 mass and the missing mass to the invariant mass should be that of a proton. This is seen in figure 4.21 where the missing mass $\gamma\gamma_{miss}^{mass}$ is plotted against the invariant mass $\gamma\gamma_{inv}^{mass}$. So we can identify $\pi^0 + p$ events without the need to detect

the proton. The $\pi^0 + p$ peak sits on top of a background distribution. By selecting the $\pi^0 + p$ events it is inevitable that some background events are interpreted falsely as $\pi^0 + p$ events. The missing particle from this background events are not protons and will probably not be seen by the SciRi detector. In the end this leads to an interpretation for inefficiency of the detector.

$$\boldsymbol{\gamma^0 + p^0} = \boldsymbol{\gamma\gamma_{inv} + \gamma\gamma_{miss}} \tag{4.4}$$

$$\boldsymbol{\gamma\gamma_{miss}} = \boldsymbol{\gamma^0 + p^0 - \gamma\gamma_{inv}} \tag{4.5}$$

$$\begin{pmatrix} Ep \\ p_p^x \\ p_p^y \\ p_p^z \end{pmatrix} = \begin{pmatrix} E_{\gamma^0} + m_{p^0} - E_{\gamma\gamma_{inv}} \\ -p^x_{\gamma\gamma_{inv}} \\ -p^y_{\gamma\gamma_{inv}} \\ E_{\gamma^0} - p^z_{\gamma\gamma_{inv}} \end{pmatrix} \tag{4.6}$$

$$\gamma\gamma^{mass}_{miss} = \sqrt{E_p^2 - p_p^2} \tag{4.7}$$

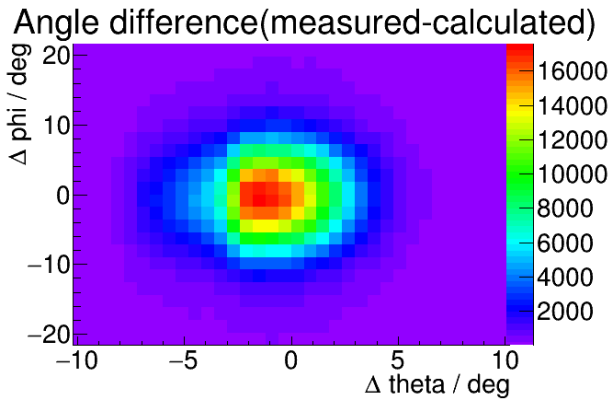

Figure 4.22: Angle difference between measured and calculated proton direction.

We assume from the distribution that around 20% of the selected events are not $\pi^0 + p$ events. In this case the missing proton to the π^0 does not exist, which leads to a calculated inefficiency in SciRi even if no proton was present. It is therefore expected that SciRi will only have a maximum efficiency of 80 %. In reality the background events could still be seen in the SciRi detector. For example in the $\pi^0 + \pi^+ + \pi^- + p$ reaction one of the charged particles could move in the same direction as the calculated missing particle from the π^0. Even though one expects no complete overlap between the $\pi^0 + p + X$ and the $\pi^0 + p$ reaction, in this section this background distribution is estimated as linear. The maximal achievable efficiency cannot be determined by the signal to noise ratio, because the influence of the $\pi^0 + p + X$ background could not be estimated. In this analysis only a minimum efficiency can be determined.

Proton reconstruction

As mentioned before, the $\pi^0 + p$ reaction is reconstructed without the need of a detected proton. The proton is calculated by the π^0 and the tagged initial photon energy E_{γ^0} using equation (4.5) with the assumption of a proton target. The mass of the calculated proton should be the proton mass. After the reconstruction of the proton a hit in SciRi is searched. The difference in the directions can be seen in figure 4.22. A clear coincidence between the measurement and the calculation is shown. The offset in the peak position is explained by an error in the position measurement of the SciRi detector. Now one can check if for every reconstructed $\pi^0 + p$ event a proton can be found in SciRi.

Efficiency

Only protons with a θ angle between 10° and 25° are used for determining the efficiency as this is the expected acceptance of SciRi. The efficiency is calculated by the ratio of protons found in SciRi and the total number of calculated protons. As mentioned before, the efficiency stated here should not be understood as a pure efficiency, but has geometrical acceptances mixed in. In figure 4.23, the number

of measured events divided by simulated events are plotted against the proton momentum. In black we have the ratio of all reconstructed $\pi^0 + p$ events. We expect a constant value over the full proton momentum range, which is not present due to background. The ratio has a minimum for proton momentum 500 to 800 MeV. The ratio is not one because the number of simulated events is smaller than the number of measured events. Still we expect that in this region we have a minimal background for the $\pi^0 + p$ reaction.

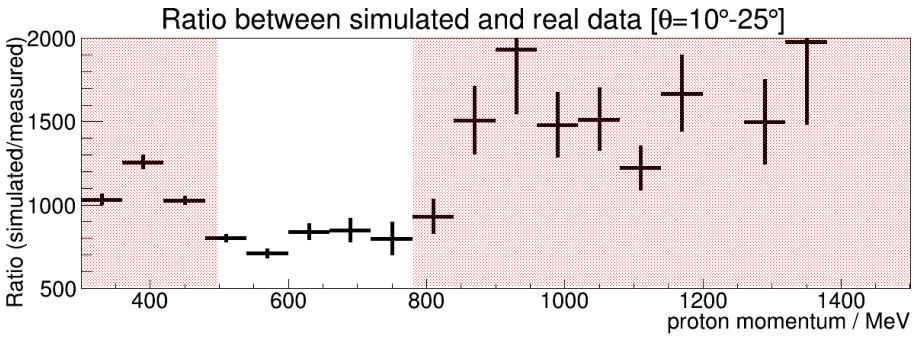

Figure 4.23: Ratio between measured and simulated data dependence on proton momentum.

The high background for high momentum protons is explained by the ratio between $\pi^0 + p$ and $\pi^0 + X$ reaction. In figure 4.24a and 4.24b the missing mass for 2γ invariant mass with different missing momentum are plotted. The vertical lines mark the cut made to select $\pi^0 + p$ events. This cut works well for low momentum protons but the missing mass distribution for high momentum protons gets broader. Even if the cuts were correct, the ratio between $\pi^0 + p$ and $\pi^0 + X$ events is smaller than for low missing momentum, leading to a higher calculated inefficiency in SciRi for high momentum. For protons with momentum between 500 and 600 MeV the background to signal ratio leads to an inefficiency of roughly 20% while for proton momentum between 1700 and 1800 this ratio is around 50%. The best noise to signal ratio is for protons with momentum between 500 MeV and 600 MeV. Events with this momentum were selected to determine the efficiency of the detector depending on the proton direction in figure 4.25.

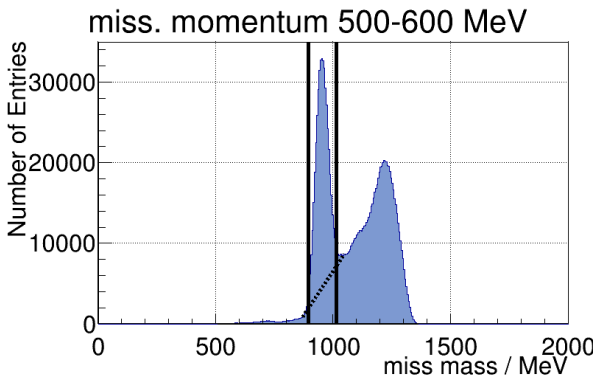

(a) Missing momentum to π^0 500-600 MeV

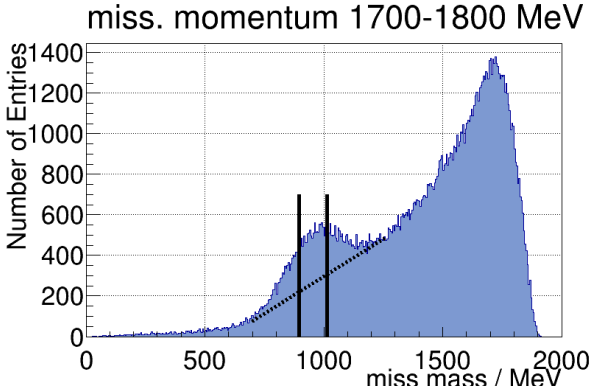

(b) Missing momentum to π^0 1700-1800 MeV

Figure 4.24: Missing mass of 2γ with different miss momentum. Verticle lines mark the selection cut for $\pi^0 + p$ events.

Two problems arise for the position efficiency. In figure 4.22 one would expect to see a rectangle with $\Delta\theta = 5°$ and $\Delta\phi = 11.25°$ width which is the angle coverage of one SciRi scintillator. The calculated proton direction is determined by the π^0 reconstructed with the BGO ball. Due to this the proton direction has a limited resolution which is in the order of roughly 5°. In extreme cases where the calculated direction points at the edge of the detector acceptance, around half of the protons are outside the acceptance. This can be seen in figure 4.25 were at the acceptance edge of $\theta = 10°$ and $\theta = 25°$ the efficiency is around 50%. While in the θ range of 15° and 20° the efficiency is constant, were the proton uncertainty is covered fully by the detector. The efficiency for $\theta = 19 - 20°$ is plotted in figure 4.26.

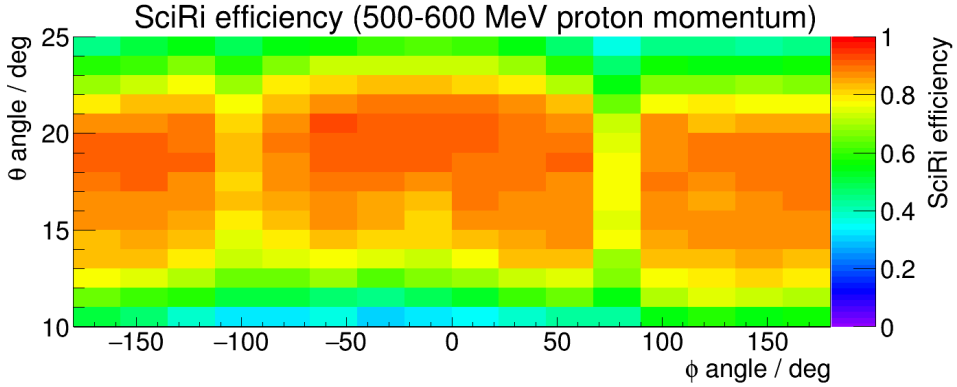

Figure 4.25: SciRi efficiency dependence on proton direction.

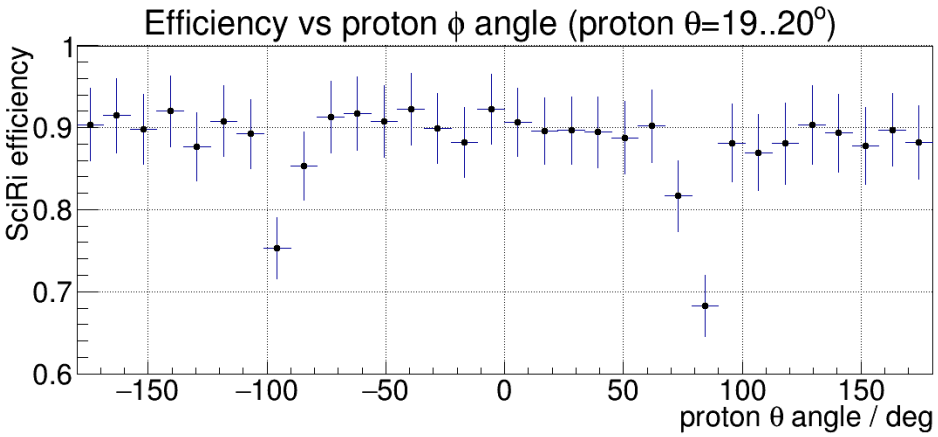

Figure 4.26: SciRi efficiency dependence on proton direction for $\theta = 19 - 20°$.

The second problem arises from the low efficiencies for $\phi = -100°$ and $\phi = 80°$ angles. The SciRi detector consists of two ring halves. The same applies for the BGO ball which can be opened for maintenance. The SciRi halves were mounted to the BGO halves. It turns out that the BGO ball cannot be closed completely, a gap of approximately 5 mm remains. This has, of course, an impact on the SciRi efficiency as the SciRi halves also have this gap.
The efficiency of the detector is around 90%. The ratio between $\pi^0 + p$ and $\pi^0 + X$ predict a maximal efficiency of around 80% meaning that the efficiency of the SciRi detector sees more protons than the expected $\pi^0 + p$ reaction allow. The reason for this are, for example, $\pi^0 + \gamma + p$ reactions which are counted

to the $\pi^0 + X$ reactions. In this example reaction there is a probability for the proton to have a similar direction as the missing particle direction calculated from the π^0. So a definite efficiency statement for the SciRi detector is not possible. From this analysis it can only be stated that the efficiency is higher than 80% over the full detector acceptance.

Time of flight

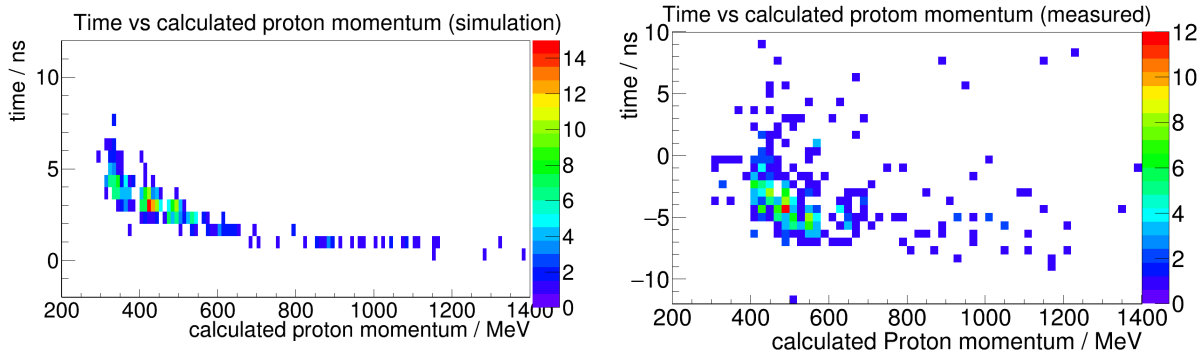

(a) Simulation.

(b) Measured.

Figure 4.27: Time of Flight for the proton against calculated momentum.

From the selected $\pi^0 + p$ events, one can try to measure the time of flight for the proton. From the calculated momentum of the proton, the velocity of the particle, and the time of flight from the target to the SciRi detector can be calculated. For this, the timewalk needs to be corrected first (see section 4.3.2). In figure 4.27a, the simulated time of flight and in figure 4.27b the measured time of flight against calculated proton momentum is plotted. While in the simulation a dependence on the momentum can be seen, no real dependence can be seen in the measured data. The time resolution of around 3.3 ns is not good enough for this kind of measurement.

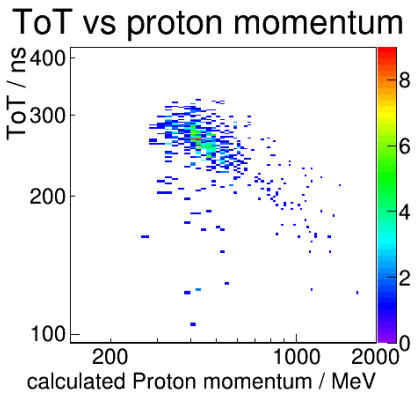

Figure 4.28: Time over threshold against calculated proton momentum for one SciRi channel.

Time over threshold

The time over threshold (ToT) is measured, as additional information to the time. With the assumption of a constant signal shape, the ToT has a relation to the amplitude of the signal, which is dependent on the energy deposit in the scintillator. This means that with the ToT an energy information could be measured. Using the selected protons from the $\pi^0 + p$ reaction, the ToT is plotted against the calculated proton momentum in figure 4.28. A ToT dependence on proton momentum can be seen. The plastic scintillator is too thin to stop protons with momentum higher 50 MeV. The ToT does not measure the full energy information of the particle. Only a fraction of the total energy is deposited in the scintillator. This is described by the Bethe-Bloch formula [17]. In figure 4.18 it is seen that the ToT distributions are different for each channel meaning that every single channel needs to be calibrated

separately. Using the Bethe-Bloch formula, the proton momentum was recalculated into the dE/dx information [17]. dE/dx is deposited energy dE in a material with thickness dx. This works only for infinitesimal thin material, as it assumes a constant and uniform energy deposition over the thickness of the material. The energy deposited in the scintillator is in reality different. Particles deposing energy in the material will get slower, which results in higher dE/dx, but is only taken into account with the Bethe-Bloch formula integrated over the material thickness. But the goal of the calibration is particle identification and not calorimetry. The calibrated ToT against calculated momentum for all channels can be seen in figure 4.29. In this picture the expected distributions for protons, π^+/π^- and K^+/K^- are drawn from the Bethe-Bloch calculation. With this ToT calibration it is possible to distinguish slow protons from minimal ionising particles like π^+/π^-. The calibration used here was a first attempt to distinguish protons from minimal ionising particles.

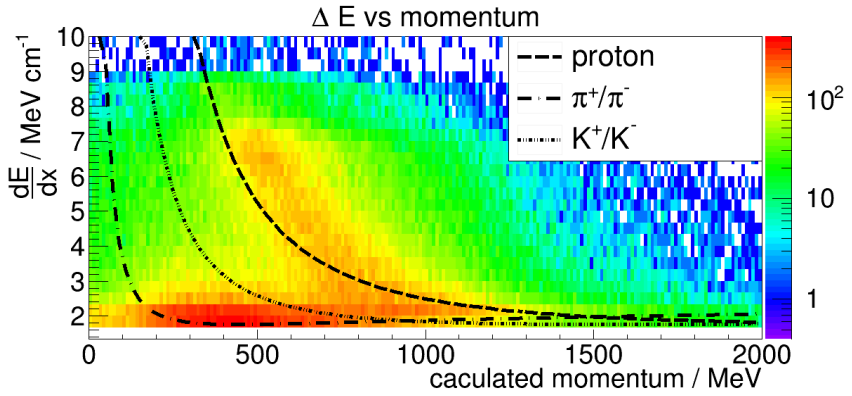

Figure 4.29: Calibrated ToT vs calculated momentum. Expected distributions for different particles using the Bethe-Bloch formula are also plotted in this picture.

4.3.5 Identified problems

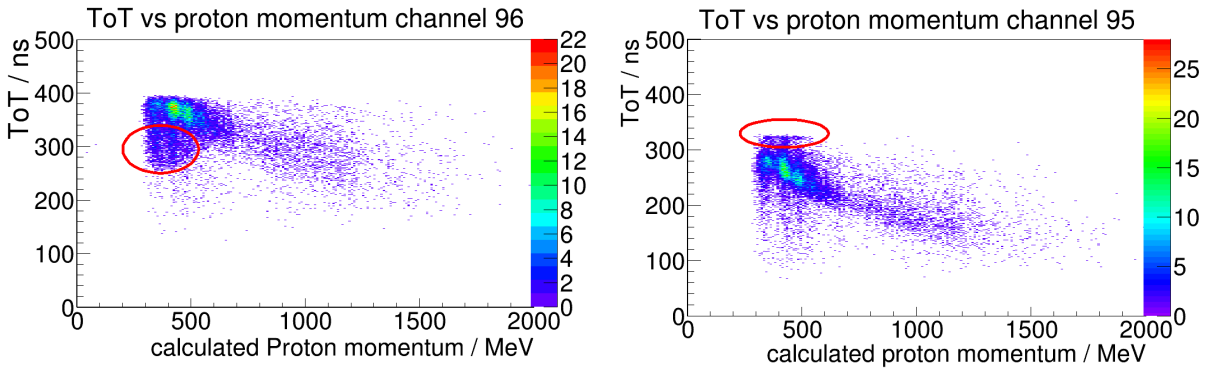

(a) Preampifier top side

(b) Preampifier bottom side

Figure 4.30: Time over threshold against calculated proton momentum. Red circle marks preampifier saturation effects.

During the commissioning of the SciRi detector, there were some small challenges which were not addressed during this thesis. The SciRi detector is mounted directly to the BGO-carbon structure and

cannot be moved perpendicular to the beam. As such all asymmetries of the BGO-carbon structure applies to the SciRi position. In this case resulting in a small ϕ dependant acceptance.
The signal after the preampifier is shaped by a capacitor in series. It turns out that the signal amplitude loss due to this cheap signal shaping method is rather high. The preampifier of the APDs were changed to produce signals with high amplitude to counter this problem. This leads to saturation of the preamplifier for low momentum protons. Those protons deposit enough energy to saturate the preamplifier. The impact of this is also strangely dependent on the side of the board on which the preamplifier circuit is located. Every preampifier board has two preampifier circuits on each side. The electronics are exactly the same, with only the location of the parts different. In figure 4.30 both effects are shown. Every channel which uses the top side of the Preampifier produces more slender signals on saturation, resulting in smaller ToT measurements. The other half of preamplifier produces signals with constant ToT. This can be easily explained with the capacitor which was used for shaping. The signal after the capacitor is the derivative of the preamplifier signal. The signal does not rise as soon the preamplifier saturates, leading to a constant ToT signal.
The problem of saturation can be solved by either lowering the ADP gain or by inserting a 1 pF capacitor into the preampifier at position C1 in figure 4.11 to reduce the amplification by a factor of 2.
The microcontroller on the SciRi Mainboard is used to communicate with the HV-Board to set the high voltages for the APDs. At the start of the beamtime communication with one microcontroller was lost. Due to this the gain of channel 1 and 2 could not be equalized together with the rest. This affects the ToT information of both channels. All channels were set to maximal gain before the communication loss which results into saturation of the preampifier rather fast and the loss off any energy information.

CHAPTER 5

Event reconstruction

SciRi was fully operational in the three week production run, 22nd June - 13th July 2015. This chapter explains the track reconstruction of the particles and from this the identification of η, η' and ω mesons and their four momenta. The reconstruction algorithm uses the ExPlORA [14] framework and was tested using the simulated events to determine the reconstruction efficiency. The influence of the BGO clustering and the SciRi detector are also examined.

5.1 Particle track reconstruction

The particle's trajectory is reconstructed by using individual hits in the detectors. In this case the BGO calorimeter and Scintillator Barrel are combined to form the central tracks. The MWPC was not included to these tracks during this thesis, but it is expected to be used in the future. MOMO, SciFi2, Drift chambers and the ToF walls are combined to form the forward tracks. In the intermediate region between the central and forward tracks the intermediate tracks are formed using the SciRi detector. The Tagger detects the bremsstrahlung electron from which the corresponding photon can be calculated. The initial state momentum is calculated from this photon and the at rest nucleon in the target similar to section 4.3.4. It can happen that the passage of a particle can activate several segments of a given detector. The first approach is to add all neighbouring hits. From this the position resolution can be improved and the correct number of initial particles can be determined. For example, a single proton going through the SciRi detector can cause two scintillator elements to register a hit. Neglecting this physical fact and not adding the hits could lead to the false interpretation that there were two particles instead of just one proton. With only one measured point of the particle trajectory one needs to assume the origin of the particle. By assuming that the particle is emitted from the target centre, the track of the particle is than reconstructed.

5.1.1 BGO clustering

Through the development of an electromagnetic shower, photons deposit their energy in multiple crystals of the BGO calorimeter. To reconstruct the photon 4 momentum, a clustering algorithm is required, which is discussed below. The objective of the clustering algorithm is to extract the energy and direction of the incident photon. The improvement of the BGO clustering was also part of this thesis, but had to be put on hold to allow for constructing the SciRi detector. Due to this postponement, the final version for the clustering algorithm is still work in progress for the BGO calorimeter. However, different approaches were tested and the impact on the meson reconstruction can be seen at the end of this thesis.

Electromagnetic shower

A photon inside a material produces an electromagnetic shower. Through bremsstrahlung, pair production, Compton scattering and positron-electron annihilation, a shower of particles is produced. Figure 5.1 illustrates the shower development. The transverse profile of a particle shower scales with the Moliere radius, R_M, which can be calculated with equation 5.1.

$$R_M = X_0 \cdot E_s / E_c \tag{5.1}$$

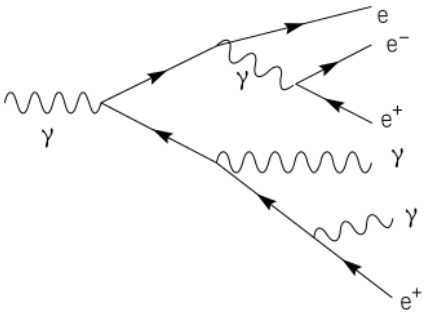

Figure 5.1: Electromagnetic shower development of a photon inside a material. [29]

Here E_s is around 21 MeV and E_c is the critical energy from the Rossi definition [17]. On average 90% of the photon energy is contained within one Moliere radius and 99% are within 3.5 Moliere radii. The radiation length of the BGO crystal is X_0 =1.12 cm and E_c =10.1 MeV which leads to a Moliere radius of R_M =2.3 cm [30], which is photon energy independent. The longitudinal shower development is dependent on the photon energy, but will not be taken into account in this section. The BGO crystals are cut into trapezoids with approximately 2 cm x 2 cm area near the target and a larger area of around 4 cm x 4 cm on the outside. This means that to first order, most of the energy can be contained within a crystal. A significant fraction of the energy, however, is distributed up to 3.5 Moliere radii around the photon entry point leading to the photon energy being distributed over a large area.

Nearest Neighbouring Clustering

One simple way to build a cluster out of the individual crystal hits is the Nearest Neighbouring Clustering. A crystal hit is defined as an energy deposition in a single crystal exceeding a user threshold, typically 3 MeV. The hit is attributed with the energy, time of energy deposition and crystal position. A single saved event has an array of crystal hits from the BGO. These arrays are then input into the clustering algorithm. The Nearest Neighbouring Clustering uses the fact that detector hits, which originate from only one particle, are in close proximity to each other. The clustering algorithm starts by adding one hit and all its neighbouring hits to the cluster. It is required that the time difference between the hits is less than 10 ns. The added neighbouring hits are than also checked for neighbours and are added to the cluster until no free neighbouring hits remain [31]. The energy, E_γ, of the photon is than the sum of all single hits energy $E(i)$, which are part of the cluster. The position of the cluster $\vec{\gamma}$ is the sum of all hits direction, $\vec{Hit}(i)$, weighed with the energy of the hits, given by equation 5.3. The square root of the energy is used for energy weighing, which results in the best position resolution.

$$E_\gamma = \sum_{i=0}^{N} E(i) \tag{5.2}$$

$$\vec{\gamma} = \frac{\sum_{i=0}^{N} \vec{Hit}(i) \cdot \sqrt{E(i)}}{\sum_{i=0}^{N} \sqrt{E(i)}} \tag{5.3}$$

This clustering algorithm was written by Tom Jude and is used for the standard analysis. The advantage of this clustering is the simplicity. It is fast, detector noise resistant and works even if the BGO crystals have different gain. The disadvantage is the inability to separate overlapping electromagnetic showers

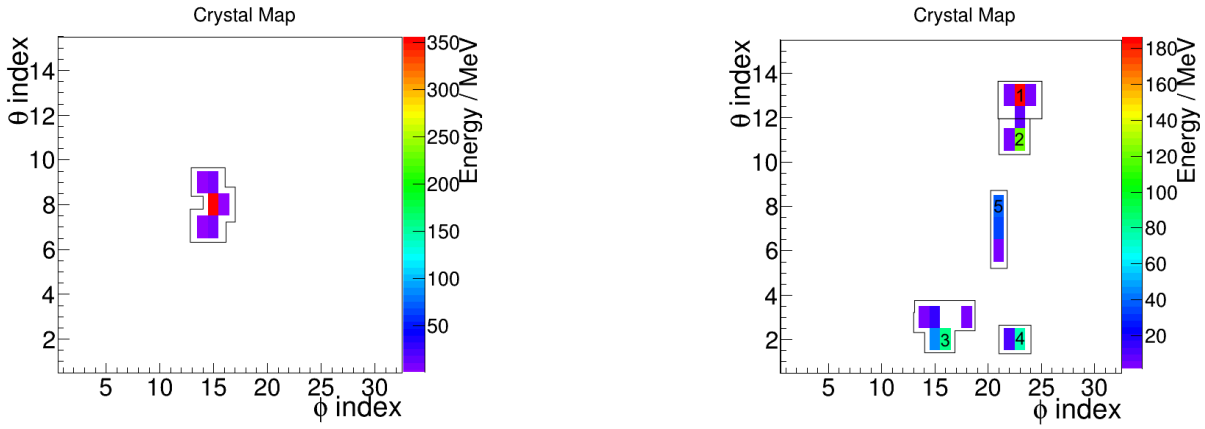

(a) (b)

Figure 5.2: BGO calorimeter θ index against ϕ index. The colour of the bins represent the deposited energy in the crystal.

from two or more photons. Most energy of the photon is contained within one or two crystals but a part of the energy is distributed over a large area of up to roughly 3x3 crystals. A example of a photon deposing energy in the calorimeter can be seen in figure 5.2a. Here the θ index of the crystal is plotted against the ϕ index. The indexing of the crystals can be seen in figure 2.3. In this 2D map of the BGO calorimeter crystals, each bin represents a crystal and the colour of the bin represents the energy deposited in the crystal. If a second photon should now hit the calorimeter in the close proximity of the first photon, it can happen that their electromagnetic shower will overlap slightly, which is depicted in figure 5.2b in the upper right of the map. In this plot five photons were simulated at the same time. This would lead to the interpretation of one missing cluster, which leads to meson detection efficiency loss with multiple photons in the final states.

Local Maxima Clustering

During the course of this thesis, the improvement of the BGO clustering was worked on. This began with the Local Maxima Clustering, which requires the information of the energy deposited in the crystals. As most energy of the photon is contained in one crystal, it is possible to make use of this fact for the clustering. First we search for local maxima, which are defined by a hit having the highest energy compared to its adjacent hits. The remaining hits are added to the nearest local maximum to form a cluster. With this it is possible to distinguish two overlapping photon showers as long they have a crystal between each other with a lower energy deposited. An example can be seen in figure 5.2b. In the upper right, photons 1 and 2 are identified separately, while the Nearest Neighbouring Clustering would add these two photons together. This clustering is also simple to implement and is only a little slower than Nearest Neighbouring Clustering algorithm. The energy deposited in the crystals is expected to be exponentially dependent on the distance to the photon entry point. The statistical nature of the shower development leads to an energy fluctuation in the crystals. On the edges of the shower, the energy deposited is low and in the order of the energy fluctuation. This can lead to formation of a local maximum, which in our case creates an additional cluster for only one photon. To reduce this background, which results in the creation of low energy cluster, an energy threshold needs to be set for a local maximum. In most cases ignoring local maxima with energy lower than 5 MeV is sufficient to reduce the misinterpretation of a cluster. In figure 5.2b photon number 3 would produce two clusters

without this threshold. The position and energy calculation from the formed clusters are calculated the same way as the Nearest Neighbouring Clustering.

Cellular Automata (GRAAL Clustering)

The BGO calorimeter was used during the GRAAL experiment which used Cellular Automata [32] for clustering. The clustering algorithm used for the GRAAL experiment was implemented after the Local Maxima Clustering. The clustering used in GRAAL is very similar to the Local Maxima Clustering. It also uses local maxima as a starting point. The difference is the association of the remaining hits to the local maxima. In the GRAAL clustering the distance and energy of the local maximum are used to calculate a probability for the hit to be associated with certain maximum. It also checks if the created clusters are overlapping showers or if these two clusters originate from one particle. In the latter case, the clusters are added together. The probability calculations describe an electromagnetic shower profile better than the Local Maxima Clustering, which results in slightly better energy and direction resolution. The position and energy calculation from the formed clusters are calculated the same way as the Nearest Neighbouring Clustering.

Cluster Fitter

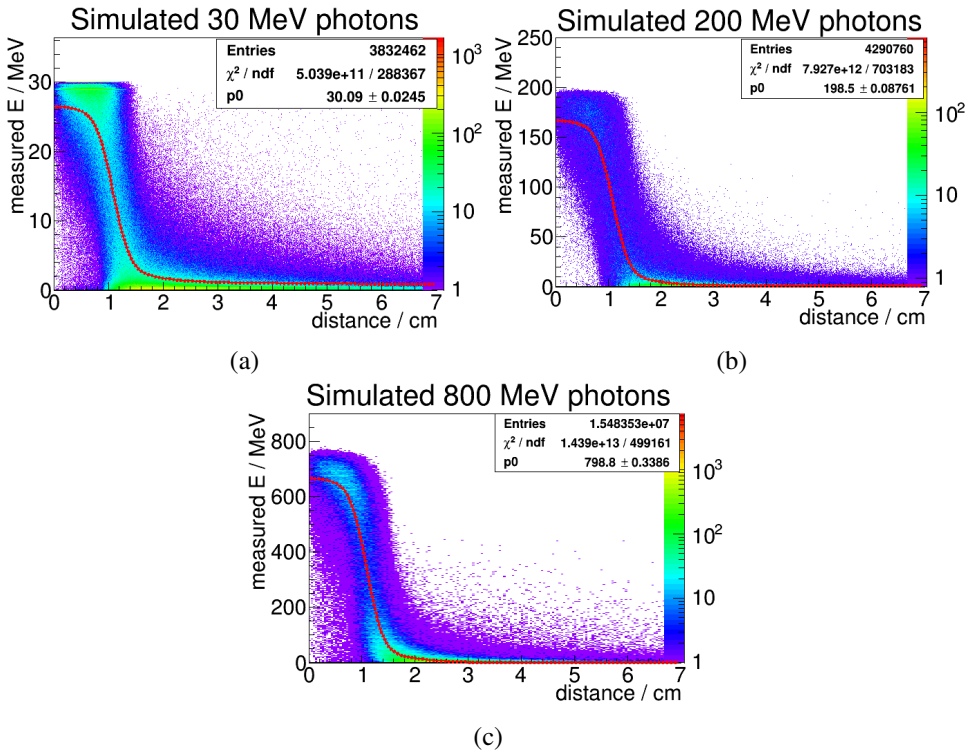

Figure 5.3: Energy deposit in crystal plotted against distance to photon direction for different photon energies.

A different idea for finding the cluster is to take the individual hits in the calorimeter and use them to fit an appropriate function which describes the transversal electromagnetic shower of the photon. The clustering algorithm presented here is not yet finalized.
The direction from the target to the crystal is projected onto a cylinder which is similar in dimensions

to the cylinder formed by the Scintillating Barrel. The cylinder is folded open to make a 2D map of the transverse shower. This map can than be used to calculate the distance between the photon direction and the individual crystal. In figure 5.3 the energy deposited in the crystal against the distance to the photon is plotted for 3 different photon energies. Here, we used simulated photons with random directions. The result is a frequency distribution of the energy-distance relation. As the electromagnetic shower model is well described in [17], it would be possible to calculate a function that uses theoretical expectations. This was not done due to the lack of time. An empirical function was found, which describes this distribution. This Cluster Fitter function, $f(x, y)$, is defined in equation (5.4). The x and y parameter are the coordinates on the 2D map. The fit parameters x_0 and y_0 determine the photon position, while the *energy* parameter determines the photon energy. In figure 5.3 the *energy* fit parameter is $p0$, which fits the simulated photon energy well. Due to the Moliere radius being independent of the photon energy, the width of the $f(x, y)$ function is also constant.

$$\begin{aligned} f(x,y) \quad = \quad & erf((\sqrt{(x-x_0)^2+(y-y_0)^2}-1.09)\cdot 3)\cdot(-energy\cdot\frac{0.69}{2}) \\ & +0.45+energy\cdot\frac{0.69}{2}+exp(-\frac{(x-x_0)^2+(y-y_0)^2}{2})\cdot\frac{energy\cdot 0.69}{2.506\cdot 5} \\ & +exp(-\frac{\sqrt{(x-x_0)^2+(y-y_0)^2}}{2\cdot\ln(energy)}) \end{aligned} \tag{5.4}$$

The Cluster Fitter was used as a standalone clustering algorithm. Here, the fit function was used to calculate the probability of overlapping electromagnetic showers. Starting with the hit with the highest energy, the $f(x, y)$ function is fitted. It is then checked whether the energy in neighbouring hits are below or above the fit function. The latter is interpreted as a different cluster which leads to the fitting of two $f(x, y)$ fit functions at the same time. After checking to see whether if the fitted functions agree with the energy deposited in the crystals, the remaining hits are added to the clusters. The association is weighted by distance and fitted cluster energy, which in this case was estimated with an exponential function. The position and energy calculation from the formed clusters are calculated the same way as the Nearest Neighbouring Clustering.
This clustering algorithm is in a preliminary stage. It was written as a proof of principle and could be used as a starting point to write a clustering algorithm which combines energy, time and position reconstruction efficiently.

Comparison of clustering in simulation

The clustering algorithms were tested using simulated data. The test with real data can be seen in section 5.5.1. The clustering algorithms are tested on their reconstruction efficiency of two photons. An efficient reconstruction of the two photons is achieved if exactly two clusters are formed. The direction of the cluster should be consistent to within 10° of the simulated photon. Additionally, the energy should not differ by more than 100 MeV. In figure 5.4 the efficiency dependence on the angle between the two photons is plotted. Nearest Neighbour Clustering starts to lose efficiency with angles lower than 40°. At this point the photon showers start to overlap which negatively impacts the efficiency in distinguishing the two photons. One way to increase the efficiency for the Nearest Neighbour Clustering is to increase the energy threshold for the crystals, which would then result in worse energy resolution. GRAAL Clustering and Local Maxima Clustering have a similar efficiency, which comes from the fact that both

clustering use local maxima to form a cluster. In comparison to the Local Maxima Clustering, the GRAAL Clustering has a lower efficiency for small angles and slightly better efficiency for large angles. The hard limit for both clustering algorithms is the opening angle of 11.25°, which is the angle difference between two neighbour crystals. The Cluster Fitter seems to have the best efficiency over all angles. It also does not have the hard limit of 11.25° like GRAAL and Local Maxima Clustering. The small angle efficiency should impact reactions with many photons in the final state, such as $\gamma + p \rightarrow p + \eta \rightarrow p + 6\gamma$. Improvement in small angle efficiency also improves the efficiency in identifying high energy mesons decaying to photons. For example, high energy π^0 decaying into two photon with a small opening angle. The maximal efficiency is not higher than 80% which stems from the applied cuts. Due to statistical fluctuation in the shower development, more clusters are formed than the number of photons. For such cases, the event is not used to determine the efficiency. Reconstruction efficiency can be increased by setting a higher energy threshold for the crystals at the lost of energy and position resolution.

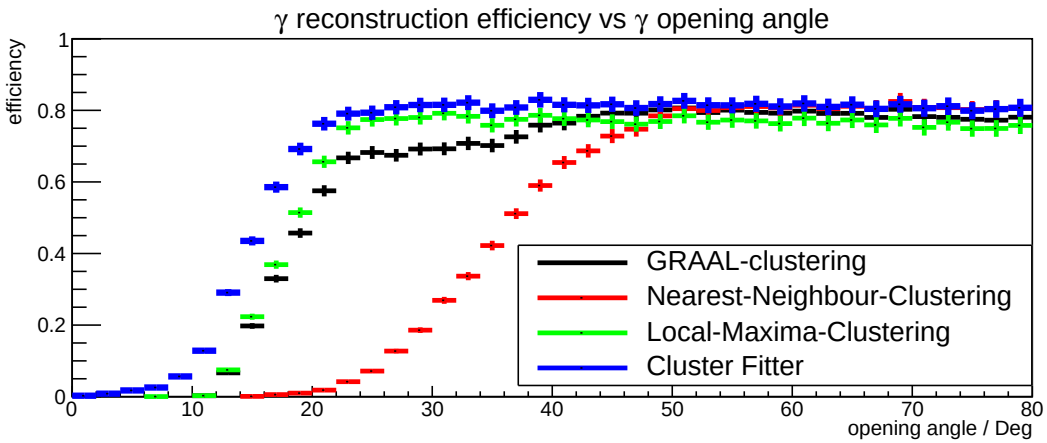

Figure 5.4: Clustering efficiency dependence on angle between two photons

5.2 Combinatorics (BTReactionFinder)

Tracks which are coincident in time are selected and given to the BTReactionFinder[1] plug-in. This plug-in uses the central, forward and intermediate tracks, and can be configured to find all possible combinations with the needed final state particle number. For example the $\gamma + p \rightarrow p + \eta \rightarrow p + 3\pi^0 \rightarrow p + 6\gamma$ reaction has seven particles at the final state, one charged and six neutral. Events with exactly seven tracks are selected. From this all possible combinations to form the $p + 3\pi^0$ final state are saved in a separate array, which are later used to select the most probable combination for the event. For each track a particle hypothesis can be set, which results in a probability calculation for the track to be the assumed particle. This was not yet used in this reconstruction, because the probability for the intermediate tracks cannot be calculated. The SciRi detector can only measure the direction of charged particles. Distinguishing between a π^+ and a proton is not possible at this point of the analysis.

[1] ExPlORA plug-in developed by Daniel Hammann, Jürgen Hannappel and Oliver Freyermuth

5.3 Reconstruction methods

The combinations formed by the BTReactionFinder are now used to reconstruct the reactions. We look through all possible combinations for one event and use only the best combination. The first selection cut is to ignore all combinations where the charge of the particle is contradictory to the assumed particle. The following selection cuts are than dependent on the measured final state.

5.3.1 Final state: $p + \pi^+ + \pi^- + 2\gamma$

In this reconstruction we want to reconstruct ω, η and η' events. The BTReactionFinder is used to find combinations of 3 charged and 2 uncharged tracks for the final state $p + \pi^+ + \pi^- + 2\gamma$. We want to reconstruct a π^0 or a η from the 2 assumed photons. The charge of the central tracks are only determined by the Scintillator Barrel. This means the assumed photons could also be other neutral particles like the neutron. With the assumption of the particles being photons, the invariant mass is plotted in figure 5.5. Two peaks can be seen on top of a continuum. At an invariant mass of around 135 MeV π^0 mesons and at around 580 MeV η mesons can be seen. These masses do not agree to the expected masses in the literature[17] due to BGO calibration, which was not optimised for high photon energies. The π^0 or η mesons are selected with an appropriate cut on the invariant mass. For the π^0 meson, the invariant mass should not differ more than 40 MeV from the peak at 135 MeV and η meson mass should not differ more than 70 MeV from the peak at 580 MeV.

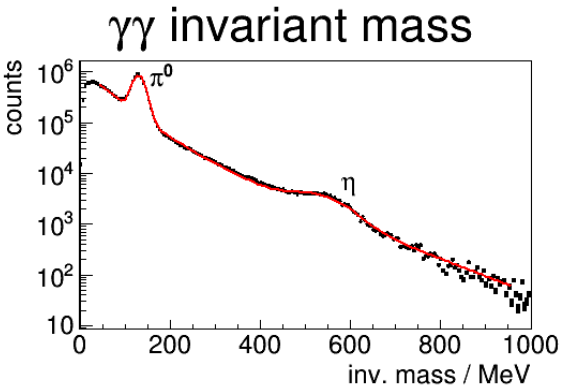

Figure 5.5: Two photon invariant mass spectrum

From the 3 charged particles, we only use the direction information. With knowledge of the initial state $\gamma + p$, the reconstructed π^0 or η and the direction $\hat{e}_i$ of the 3 charged particles, i, we can calculate the momentum, p_i, for the 3 charged particles, i, using the momentum conservation in equations (5.7), (5.8) and (5.9). A is the sum of known 4-momenta given by equation (5.5).

$$\begin{aligned} \gamma' + p' &= \pi^0 + \pi^+ + \pi^- + p \\ \gamma' + p' - \pi^0 &= A = \pi^+ + \pi^- + p \qquad (5.5) \\ \vec{A} &= p_{\pi^+} \cdot \hat{e_{\pi^+}} + p_{\pi^-} \cdot \hat{e_{\pi^-}} + p_p \cdot \hat{e_p} \qquad (5.6) \end{aligned}$$

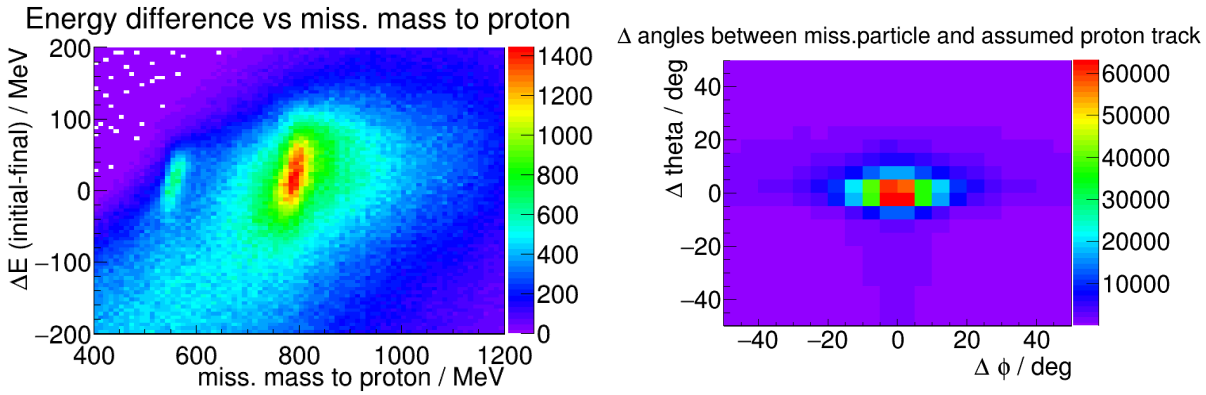

(a) Energy difference against missing mass to the assumed proton for the $p + \pi^+ + \pi^- + \pi^0$ reconstruction.

(b) Direction difference between missing and measured proton direction

Figure 5.6

$$p_{\pi^+} = \frac{A^x(e_p^z e_{\pi^-}^y - e_p^y e_{\pi^-}^z) + e_p^x(A^y e_{\pi^-}^z - A^z e_{\pi^-}^y) + (A^z e_p^y - A^y e_p^z)e_{\pi^-}^x}{e_p^x(e_{\pi^-}^z e_{\pi^+}^y - e_{\pi^-}^y e_{\pi^+}^z) + e_{\pi^-}^x(e_p^y e_{\pi^+}^z - e_p^z e_{\pi^+}^y) + (e_p^z e_{\pi^-}^y - e_p^y e_{\pi^-}^z)e_{\pi^+}^x} \tag{5.7}$$

$$p_{\pi^-} = -\frac{A^x(e_p^z e_{\pi^+}^y - e_p^y e_{\pi^+}^z) + e_p^x(A^y e_{\pi^+}^z - A^z e_{\pi^+}^y) + (A^z e_p^y - A^y e_p^z)e_{\pi^+}^x}{e_p^x(e_{\pi^-}^z e_{\pi^+}^y - e_{\pi^-}^y e_{\pi^+}^z) + e_{\pi^-}^x(e_p^y e_{\pi^+}^z - e_p^z e_{\pi^+}^y) + (e_p^z e_{\pi^-}^y - e_p^y e_{\pi^-}^z)e_{\pi^+}^x} \tag{5.8}$$

$$p_p = \frac{A^x(e_{\pi^-}^z e_{\pi^+}^y - e_{\pi^-}^y e_{\pi^+}^z) + e_{\pi^-}^x(A^y e_{\pi^+}^z - A^z e_{\pi^+}^y) + (A^z e_{\pi^-}^y - A^y e_{\pi^-}^z)e_{\pi^+}^x}{e_p^x(e_{\pi^-}^z e_{\pi^+}^y - e_{\pi^-}^y e_{\pi^+}^z) + e_{\pi^-}^x(e_p^y e_{\pi^+}^z - e_p^z e_{\pi^+}^y) + (e_p^z e_{\pi^-}^y - e_p^y e_{\pi^-}^z)e_{\pi^+}^x} \tag{5.9}$$

With the momentum fully known, we need to assign the mass to the charged particles. One of these charged particles should have the proton mass while the other should have the charged π mass. This means we have 3 possible combinations which were filled into the plot in figure 5.6a for the $p + \pi^+ + \pi^- + \pi^0$ reconstruction. In this plot one can see the energy difference between initial and final state against the missing mass to the assumed proton. Energy difference zero means energy conservation. In this case the missing mass to the proton shows a η and ω peak. From all possible combinations the combinations with the best energy conservation is selected. With this we now have fully reconstruct the $p + \pi^+ + \pi^- + \pi^0/\eta$ final state. The results from this reconstruction can be found in section 5.3.3 for simulated events and in section 5.4 for real beam data.

5.3.2 Final state: $p + 6\gamma$

In this reconstruction we use the final state $p + 6\gamma$ to identify η and η' meson. All events with 1 charged track and 6 uncharged track are selected. The 6 uncharged tracks are assumed to be photons and the two photon invariant mass is calculated for every possible combination. This invariant mass plot is seen in figure 5.5. Combinations are selected were it is possible to reconstruct $3\pi^0$ or $2\pi^0 + \eta$ out of the 6γ. With the sum of the reconstructed mesons the missing mass is calculated. The missing mass should be that of the proton and in the same direction as the measured charged track. The direction difference is plotted in figure 5.6b. The event is selected if and only if the measured and calculated direction agree up to 12° and the mass of the calculated proton does not differ more than 70 MeV from the literature value. The momentum of the proton calculated from the reconstructed mesons is then associated to the charged

track and is now interpreted as a proton. Now the $p+3\pi^0$ or $p+2\pi^0+\eta$ reactions are reconstructed. The results from this reconstruction can be found in section 5.3.3 for simulated events and in section 5.4 for real beam data.

5.3.3 Simulated reconstruction efficiency

The simulation was used to test the reconstructions. With this the reconstruction efficiency of the algorithm could also be estimated. 100000 $p+\eta$, $p+\eta'$ and $p+\omega$ events were simulated. The reactions were fully reconstructed and in all reconstructions the momentum of the proton is calculated from the reconstructed meson. This means that the missing mass to the proton is equal to the invariant mass of the meson. The missing mass to the proton was used for plots instead of the invariant mass of the meson, because the angle resolution for the meson is worse than for the proton. The worse angle resolution of the meson is due to the meson being composed out of multiple particles, in which case the angle uncertainties are added together. So even through the missing mass is presented in the plots the meson is not missing and as mentioned before the missing mass to the proton represents the reconstructed meson mass. This applies to all following plots. In figures 5.7, 5.9 and 5.8 the results of the reconstruction from section 5.3 are shown. Plotted in the figures is the missing mass to the proton, calculated using the equation (5.12), for the reaction stated in the title.

$$\gamma^0 + p^0 = p + meson \tag{5.10}$$

$$meson = \gamma^0 + p^0 - p \tag{5.11}$$

$$\text{miss. Mass to proton} = |\gamma^0 + p^0 - p| \tag{5.12}$$

The reconstruction efficiency without the SciRi detector is shown in black. In this case only the central and forward detector were used to reconstruct the events. The reaction counts as reconstructed, if the mass of the meson is reconstructed in the missing mass spectrum. The masses of η, η' and ω can be found in table 3.1. Due to energy and angle resolutions, the calculated meson mass is not exact, which leads to a broadening in the mass resolution. In the legend of each plot, the number of reconstructed events were determine by the area of the used fit function for the peak. A Voigt function, a convolution of a Gaussian and a Breit–Wigner distribution, was used to fit the peak. The error of the reconstructed event number, N, is the standard statistical error $\sqrt{N}$. By inspecting the peak position in the reconstructed events, it is seen that they are not at the correct mass. This is due to preliminary energy calibrations.

Reaction	BR / %	Max. Events w/ SciRi	Max. Events w/o SciRi	Ratio $\frac{w/}{w/o}$ SciRi
$p+(\eta \to \pi^+ + \pi^- + \pi^0)$	22.5	15800±100	4950±70	3.2±0.05
$p+(\eta \to 3\pi^0)$	31.6	12400±100	5150±80	2.4±0.04
$p+(\eta' \to \pi^+ + \pi^- + \eta)$	16.9	8600±100	2000±40	4.3±0.1
$p+(\eta' \to 2\pi^0 + \eta)$	8.2	1510±40	620±20	2.4±0.1
$p+(\omega \to \pi^+ + \pi^- + \pi^0)$	88.3	34700±200	8300±100	4.2±0.05

Table 5.1: Expected detectable events for full setup and setup without SciRi detector.

In the simulation all decay channels were allowed. In table 5.1 the expected branching ratio (BR) is stated for each decay channel. Due to different acceptances for the final state particles, it is not possible to reconstruct all events (see section 3.2). In the same table the maximal detectable event number is also stated for the full BGO-OD detector and BGO-OD without the SciRi detector. The calculation of these values was done by cuts similar to section 3.3 and should not exceed the branching ratio for the decay.

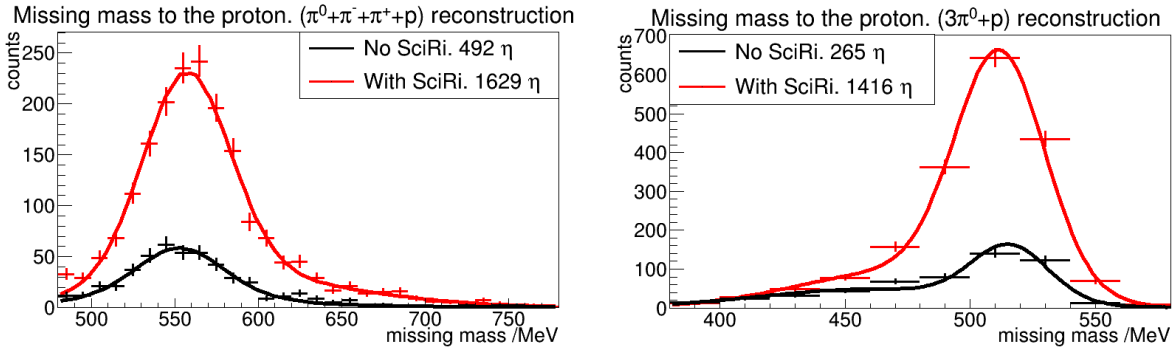

(a) (b)

Figure 5.7: Reconstruction of 100000 simulated $p + \eta$ events. The red line marks the reconstruction using the full setup and in black only forward and central detectors were used.

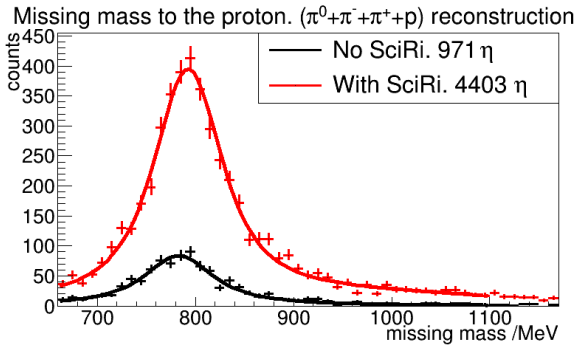

Figure 5.8: Reconstruction of 100000 simulated $p + \omega$ events. The red line marks the reconstruction using the full setup and in black only forward and central detectors were used.

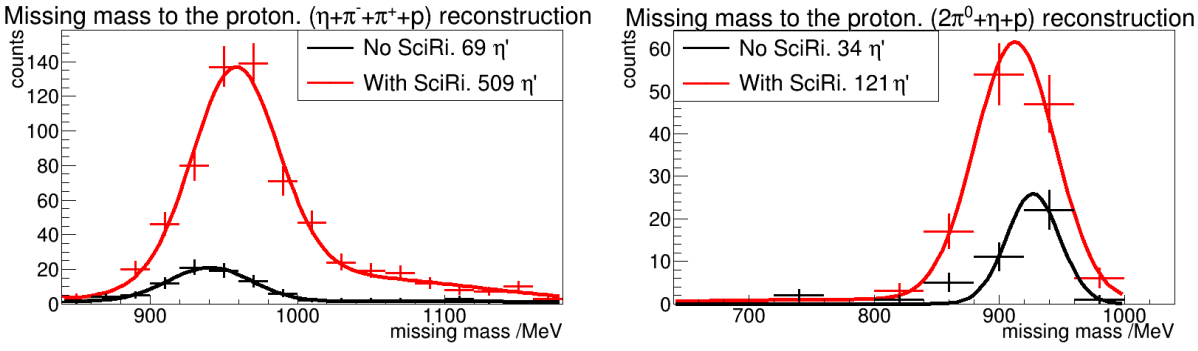

(a) (b)

Figure 5.9: Reconstruction of 100000 simulated $p + \eta'$ events. The red line marks the reconstruction using the full setup and in black only forward and central detectors were used.

Reaction	w/ SciRi / %	w/o SciRi / %	Reconstructed events $\frac{w/}{w/o}$ SciRi
$p + (\eta \to \pi^+ + \pi^- + \pi^0)$	10.3±0.1	10.0±0.1	3.3±0.2
$p + (\eta \to 3\pi^0)$	11.5±0.1	5.0±0.07	5.5±0.4
$p + (\eta' \to \pi^+ + \pi^- + \eta)$	6.0±0.08	3.4±0.06	7±1
$p + (\eta' \to 2\pi^0 + \eta)$	8.0±0.09	5.5±0.07	3.5±0.7
$p + (\omega \to \pi^+ + \pi^- + \pi^0)$	12.7±0.1	11.7±0.1	4.5±0.2

Table 5.2: Algorithm reconstruction efficiencies for the expected number of events.

Here we also compare the possible number of detectable events with and without the SciRi detector. Without SciRi we only use the acceptances of central and forward detector, while in the case of with SciRi we also take the SciRi acceptance for charged particles into account. The ratio of this shows that we can expect around 4 times more $\pi^+ + \pi^- + 2\gamma + p$ events and around 2.5 more $6\gamma + p$ events. This again shows that the acceptance covered by the SciRi detector is crucial for event reconstruction.
The reconstructed events are compared to the maximal possible event number. Determined event reconstruction efficiencies are seen in table 5.2. Overall the efficiency is between $3 - 12\%$ which means we cannot reconstruct approximately 90% events. One reason for this is the detector acceptance. Due to gaps between the detector segments, the detector acceptance is smaller than the applied cut for calculating the maximal possible event number. Additionally the clustering and track reconstruction is not always correct. It can happen that especially for the $6\gamma + p$ event, two of the photon shower overlap and cannot be distinguished any more (see section 5.1.1). Additionally, if a particle hits the acceptance edge between the BGO ball and SciRi it can happen that in both detectors energy is deposited and two tracks are reconstruct from only one particle. Extra tracks are not used right now for reconstruction and the whole event is ignored. It is not clear why the $p + \pi^- + \pi^+ + \eta$ reconstruction has a factor 2 lower efficiency than the $p + \pi^- + \pi^+ + \pi^0$ reconstruction. This could mean that the reconstruction efficiency for $\eta \to 2\gamma$ is lower than $\pi^0 \to 2\gamma$. Comparing the expected and reconstructed ratios of events with and without SciRi, one sees that the reconstruction has always a higher ratio. This comes from the fact that the used acceptance of $\theta < 10°$ for the forward spectrometer is not present for all ϕ angles. This means that the real acceptance is smaller than the estimated, which leads to a higher ratio in the reconstruction.

5.4 Real data

In this section, the 3-week production run (22nd June - 13th July 2015) beamtime was used to reconstruct the events with real data. In the following plots the missing mass to the proton was used instead of the invariant mass of the meson, which is explained in section 5.3.3. The results of the reconstruction with the full detector can be seen in figure 5.10, 5.11, 5.12 and 5.13 marked by the red line. It was possible to reconstruct all selected reactions. The reconstructed event number is always taken from the peak fit. The error on this number N is always the standard statistical error $\sqrt{N}$.
In the real data a background is present, which was estimated with a Gaussian function. This was used to subtract the background events from the total distribution to determine the number of the reconstructed mesons. The present background can be reduced using the time over threshold information measured by the SciRi detector. It was possible to calibrate a relation between deposited energy and measured ToT, which can be used to select slow moving protons. In figure 4.29 the calibrated energy against particle momentum is shown. The $\pi^+ + \pi^0 + \pi^- + p$ reconstruction when the proton was found in SciRi is plotted in figure 5.14a. Using the same data, slow protons were selected by using the ToT information

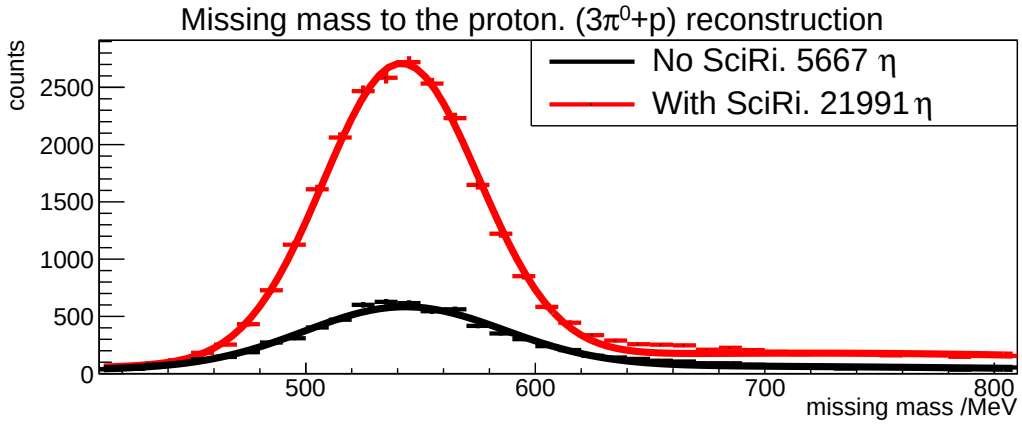

Figure 5.10: $p + 3\pi^0$ reconstruction dependence on SciRi

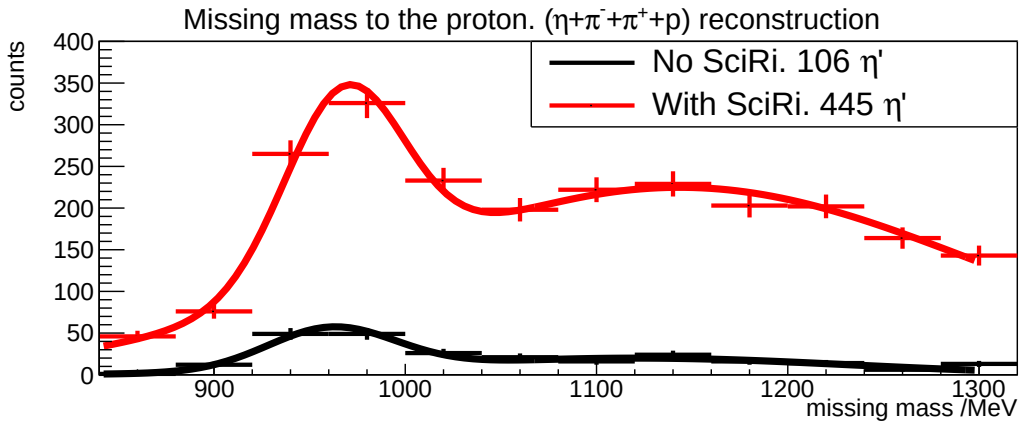

Figure 5.11: $p + \pi^+ + \pi^- + \eta$ reconstruction dependence on SciRi

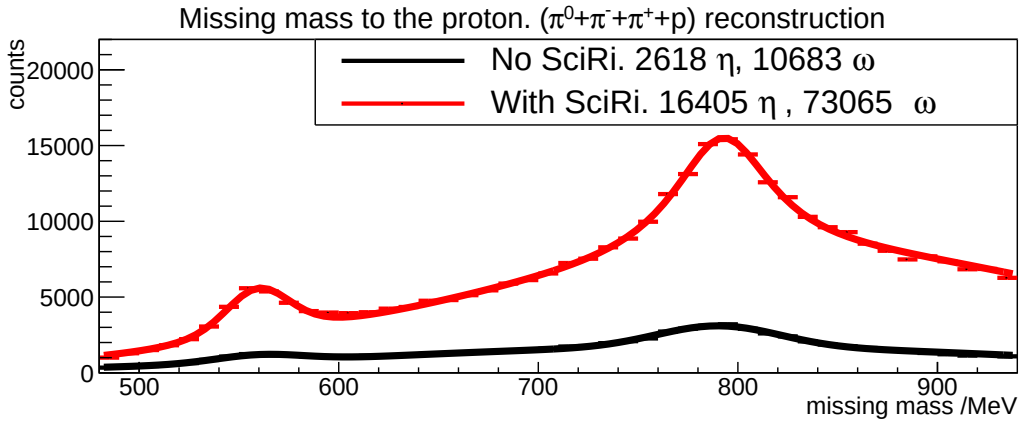

Figure 5.12: $p + \pi^+ + \pi^- + \pi^0$ reconstruction dependence on SciRi

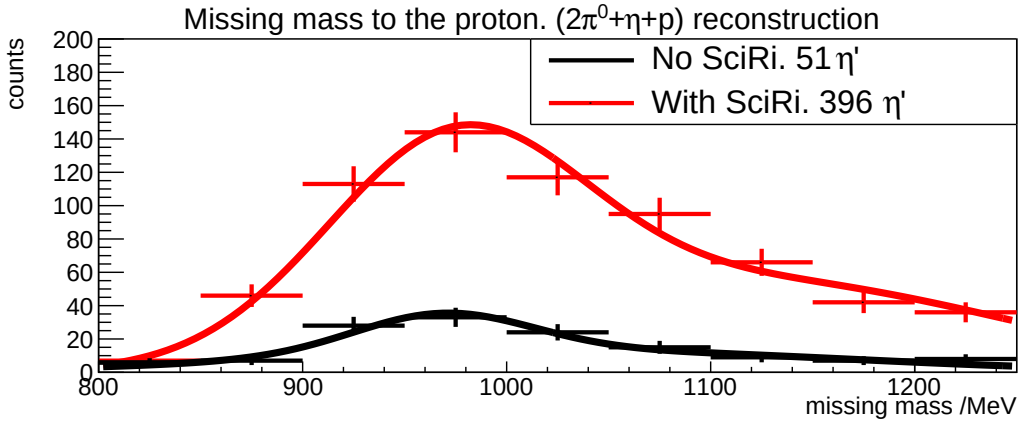

Figure 5.13: $p + \eta + 2\pi^0$ reconstruction dependence on SciRi

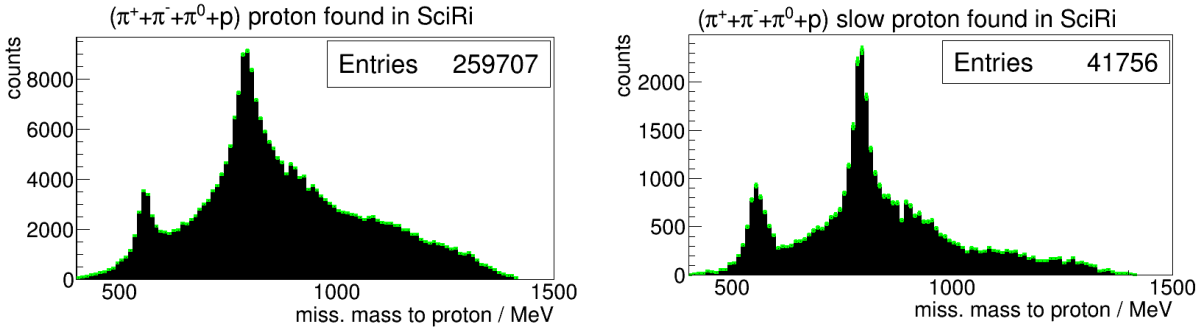

(a) Proton found in SciRi.

(b) Selected slow protons in SciRi.

Figure 5.14: Missing mass to the proton from the $\pi^- + \pi^+ + \pi^0 + p$ reaction.

in figure 5.14b. This reduces the background, but at the cost of a high number of statistics. Still it is possible to reduce the background using the ToT information. In figure 5.15 and 5.16 the same was done for the η' channels. Especially in the $\eta' \rightarrow 2\pi^0 + \eta$ channel in figure 5.16a it is not clear if a η' peak is on top of a background or if it is only background peaking in the η' mass. But looking at figure 5.16b after the cut, it is now possible to distinguish η's from background. The difference in mass resolution between the two η' channels stems mainly from the reconstruction. In the $\pi^+ + \pi^- + \eta + p$ reconstruction, only the energy of the two photons is measured with the BGO calorimeter, while the remaining particle momentum is calculated. On the other hand the $2\pi^0 + \eta + p$ reconstruction needs to measure the energy of six photons. This leads to an energy uncertainty of a factor 3 compared to the $\pi^+ + \pi^- + \eta + p$ reconstruction and results in worse mass resolution.
During the following analysis the cut on slow momentum protons was not applied to have comparable results, as this cut cannot be applied to the central or forward detector in the same way.

5.5 Impact of BGO clustering and SciRi on the reconstruction

In the course of this thesis, changes on the BGO clustering and the increase of the BGO-OD acceptance with the new SciRi detector were made. In this chapter we now want to look at the impacts of these changes. First the BGO clustering algorithms are tested with real data. Lastly the impact of the SciRi

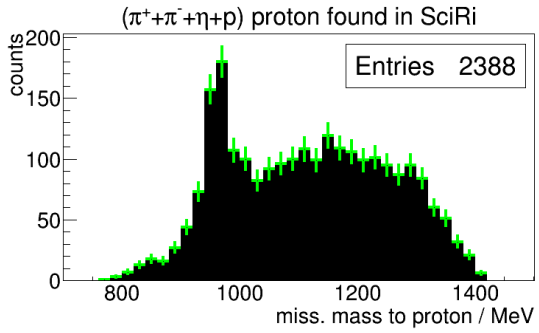

(a) Proton found in SciRi.

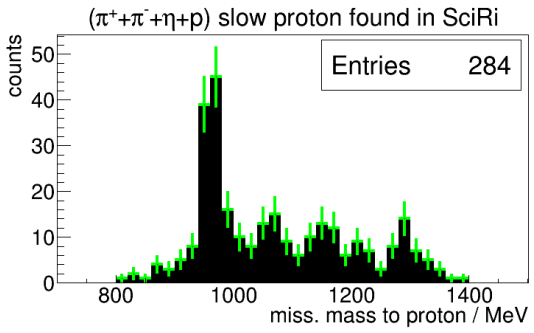

(b) Selected slow protons in SciRi.

Figure 5.15: Missing mass to the proton from the $\pi^- + \pi^+ + \eta + p$ reaction.

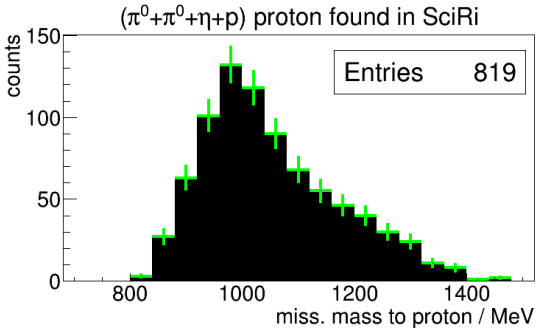

(a) Proton found in SciRi.

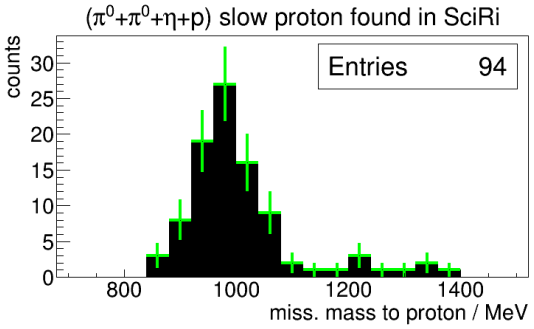

(b) Selected slow protons in SciRi.

Figure 5.16: Missing mass to the proton from the $\eta + \pi^0 + \pi^0 + p$ reaction.

detector is looked at.

5.5.1 BGO clustering

The introduced BGO clusterings from section 5.1.1 are used in this section to compare them. In contrast to the simulation, noisy BGO channels exist in real data. If the clustering losses reconstruction efficiency due to the noise, a lower number of events could be reconstructed. In figure 5.17 and 5.18 the missing mass to the proton for different clustering algorithms is shown using the same data. From the $3\pi^0 + p$ reaction in figure 5.17b we see the influence of overlapping clusters which were mentioned in section 5.3.3. It was expected that the Nearest Neighbour Clustering will have a low reconstruction efficiency due to overlapping clusters. In this case only around 50% of the events could be reconstructed compared to other clustering methods. The Cluster Fitter could reconstruct the most events for this reaction. From the $2\pi^0 + \eta + p$ reaction in figure 5.18b, one would actually expect a similar result. It seems however that the GRAAL clustering has a problem to split overlapping clusters and produces similar results to the Nearest Neighbour Clustering. The electromagnetic showers of the $\eta \to 2\gamma$ decay tend to overlap more often then the $\pi^0 \to 2\gamma$ decay, due to higher a Lorentz boost. Looking at the reconstructed event number in the $\pi^+ + \pi^- + \pi^0 + p$ reconstruction in figure 5.17a we see a different result. For the neutral meson decays, the Nearest Neighbour Clustering produces good results. With only two photons, the probability for overlapping shower is small. Again we see that the GRAAL clustering has different results than the Local Maxima clustering. The reason could be that the GRAAL clustering is not optimized for the BGO-OD setup. The fact that the Cluster Fitter has similar results is not surprising. This

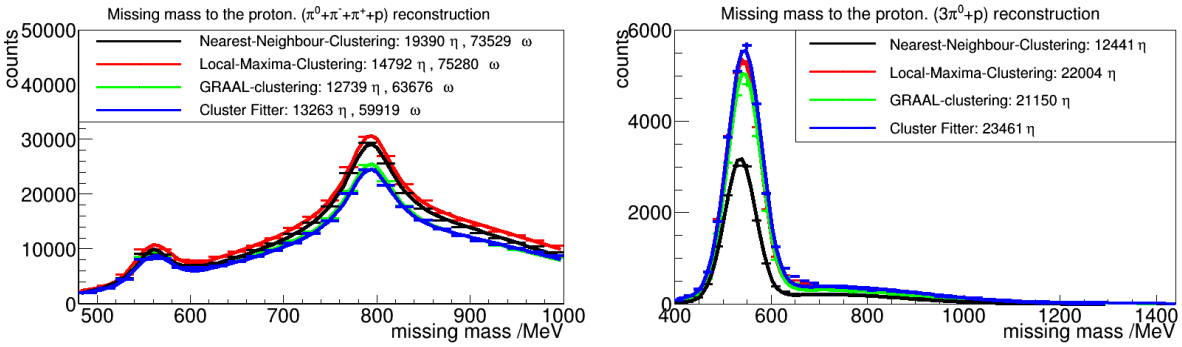

(a) (b)

Figure 5.17: Initial photon energy E_γ against theta angle of proton. Decay particles of the meson within detector acceptance.

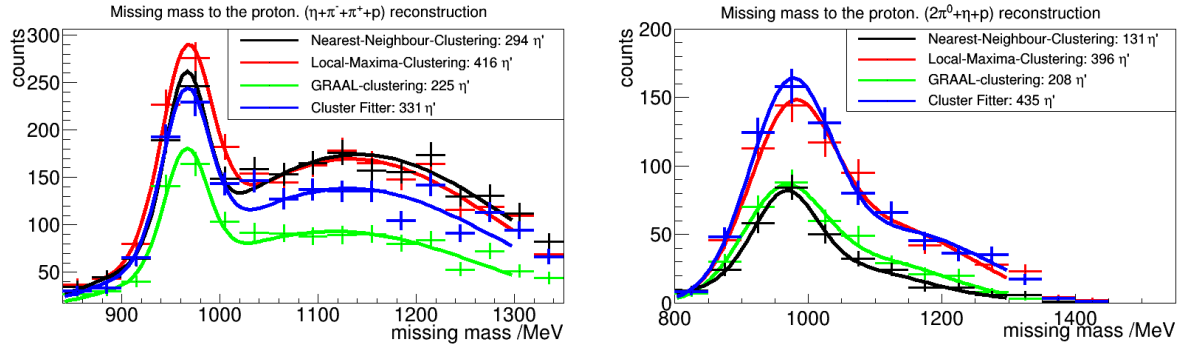

(a) (b)

Figure 5.18: Initial photon energy E_γ against theta angle of proton. Decay particles of the meson within detector acceptance.

clustering was written with the intent of photon reconstruction. However in this case we also have π^-, π^+ and protons at the final state, which do not produce an electromagnetic shower. In the $\pi^- + \pi^+ + \eta + p$ reconstruction on the other hand, the Cluster Fitter seems to work better, because the photons from the η decay tend to overlap.
In conclusion, the Local Maxima Clustering seems to reconstruct a high number of events independent of the reaction. This clustering was used during all reconstructions in this thesis where the BGO clustering was not specifically mentioned. Even though the Cluster Fitter is still in the test period, it could reconstruct events events comparable to the other clustering methods. As soon the Cluster Fitter is optimized it should produce even better results than presented here.

5.5.2 SciRi

In this section we now compare the results of the new SciRi detector. The expectations from the simulation can be found in section 5.3.3. Here we look at the results with real data. The same data with and without SciRi are used for the comparison. In figure 5.10, 5.11, 5.12 and 5.13 the situation before the construction of SciRi is drawn by a black line and red describes the full detector setup.
In figure 5.10 we see the results for the $3\pi^0 + p$ reconstruction. With the use of the SciRi detector we can

reconstruct 3.9±0.1 times more events. In the simulations we expected that the reconstruction would have 5.5±0.4 more events, which was already contradictory to the geometrical ratio of 2.4±0.04. But in section 5.5.1 we also saw that the results for this reconstruction vary with BGO clustering. Without SciRi the proton can be found half of the time in the BGO calorimeter, from which the clustering efficiency determines the number of reconstructed events. It seems that in the real data, the background, which is partly produced by neutrons from the electron beam dump, disturbs the reconstruction. Still, the expected ratio between SciRi and no SciRi situation from the geometry is even smaller than the measured ratio, which stems from the fact that the acceptance of the forward spectrometer is smaller than 10° in θ.
A totally contradictory picture is shown in figure 5.13 for the $2\pi^0 + \eta + p$ reaction. Here we should have the same problems as mentioned before for the $3\pi^0 + p$ reaction. But here we have a SciRi and no SciRi ratio of 8±3 which is much higher than the expected ratio of 3.5±0.7 and the geometrical ratio of 2.4±0.1. But due to the high statistical error, no conclusion can be made yet. It could be that the background was not correctly subtracted and the determined event number was wrong.
The $\pi^+ + \pi^- + \pi^0 + p$ reconstruction in figure 5.12 shows a ratio 6.3±0.3 for η and 6.8±0.2 for ω. This is much higher than the expected ratios. In ω event number determination, the peak is on top of the background peak, which leads to problems in background subtraction. So this could be a result of wrong background subtraction. Looking at the $\pi^- + \pi^+ + \eta + p$ reconstruction in figure 5.11 we see a ratio of 4.2±0.9. Like in the $2\pi + \eta + p$ reaction, we cannot estimate the background that well due to low statistics. The estimated ratio from the geometry of 4.3±0.1 however seems to agree with the real data.
All determined ratios, show better results than the geometrical ratios. We conclude that the SciRi detector works as expected. The discrepancy in the ratio is explained by detectors which have a small noise problem and subtraction of background. The SciRi detector had almost no noise which lead to higher ratios than in simulation. The SciRi detector will play a very important roll in the future physics proposals, vastly improving statistics for many investigated reaction channels.

CHAPTER 6

Conclusion and Outlook

The goal of this thesis was the reconstruction of mesons with the BGO-OD detector and making any necessary improvements. When I began this master thesis project, there was a big acceptance hole between 10° to 25°, which reduced the event reconstruction efficiency significantly. To cover this region in as short a time as possible, a Scintillating Ring (SciRi) detector was constructed, calibrated and implemented as is described in this thesis. The SciRi detector is a 96 channel plastic scintillator ring detector with an Avalanche Photodiode (APD) readout. It can be used to detect charged particles. The scintillator material was obtained from parts of an old detector, which were being stored in a warehouse, and the APDs were provided by the Crystal Barrel experiment. It was possible to construct the detector within a short amount of time and thereby reduce costs. In addition to the APDs, the Crystal Barrel experiment also gave us the matching preamplifier and high voltage set board. The preamplifier was constructed especially for the Crystal Barrel calorimeter crystals, which have a different light yield and also emit light over a longer period of time than the plastic scintillator used in SciRi. The preamplifier was accordingly modified to accommodate the smaller APD signals. With the help of Thomas Zimmermann and Jürgen Hannappel, additional electronic boards were constructed to use the boards provided from Crystal Barrel for the SciRi detector. The detector was tested during the July 2015 beam time with the $\gamma + p \rightarrow p + \pi^0$ reaction and was also used at the same time to take data. The tests further showed that the detector was operational and that it is possible to measure the deposited energy in the scintillator to distinguish slow protons from minimum ionising particles. By reconstructing $p+\eta$, $p+\eta'$ and $p + \omega$ reactions, it was possible to increase the number of events by at least a factor 3 with the SciRi detector, which confirms the expected gain by covering the acceptance gap. The momentum of the particles detected in SciRi were calculated by momentum conservation for the analysis.

Particles that deposit their energy in a calorimeter are identified by the formation of a cluster formed by individual crystals. Photons deposit energy inside the material by developing an electromagnetic shower. If the showers overlap in a calorimeter, it can markedly reduce the particle reconstruction efficiency. The BGO calorimeter is the only detector that can detect photons in the BGO-OD detector. This means an increase in particle reconstruction efficiency leads directly to a higher reconstructed number of events, where the meson decay includes photons. For this thesis, a first attempt to improve the BGO clustering was done. With the Local Maxima Clustering algorithm, it was possible to reconstruct approximately 50% more $p + 6\gamma$ events in comparison to the previous clustering analysis. The Cluster Fitter can distinguish overlapping cluster even better, but is not optimised for charged particles. This clustering software is still under construction, but shows that the principle is working. With this the first steps to the optimal BGO clustering algorithm were done.

Our goal was reached as evidenced by the successful reconstruction of meson photoproduction. The new SciRi detector is operational and performed well. The acceptance of the SciRi detector can be increased from $10° < \theta < 25°$ to $8° < \theta < 25°$. This could be achieved by cutting new inner ring scintillators, which would be approximately 2 cm longer than the original version. Through this augmentation,

the overlap between the SciRi detector and forward detector would be enhanced. In this overlapping region, the detection efficiency will further be improved. The additional material of 2 cm scintillator in the beam direction, which now would cover a part of the forward detector acceptance, should not lead to undue scattering. This overlap would further prevent any acceptance gaps from appearing, should the detectors not be perfectly aligned. In addition, the acceptance would fit the multigap resistive plate chamber (Daisy) detector acceptance. The disadvantage is a slightly worse θ position resolution in the inner SciRi ring.
The SciRi detector would complement the multigap resistive plate chamber (Daisy), which will be installed soon after the writing of this thesis. It is still under investigation whether the SciRi detector disturbs the Daisy detector more than it helps, but there are several advantages in pursuing this idea. Without SciRi, the Daisy detector would have to assume that the detected particle origins from the target. A second detector would help to identify detector noise and reconstruct the particle track. With the Daisy time resolution of approximately 50 ps, it would then be possible to measure the time of flight. The combination with the measured energy in SciRi could subsequently be used to identify the particle and hence the time of flight could be used to calculate the momentum of slow moving particles. SciRi affords a redundancy that will serve to improve the measurement of the particle's 4-momentum.

CHAPTER 7

Acknowledgements

In this chapter I would like to thank all who supported me during my thesis. I would like to thank Prof. Schmieden for giving me a thesis which includes aspects from hardware and analysis. I would like to thank Prof. Phil Cole for reading my thesis and giving me suggestions for improvements. Also being my evaluator for this thesis.
I thank Dr. Jürgen Hannappel for his advice on the SciRi construction and support during each step of the construction. The construction of the SciRi detector was only possible with the support from the Crystal Barrel experiment. I would like to especially thank Martin Urban and Cristian Honisch for their support on the Avalanche Photodiode.
Thanks to Thomas Zimmermann for the design of the additional electronic boards, which allowed the implementation of the electronics from the Crystal Barrel experiment into SciRi. I also give thanks to the workshops of the physics institute, which could construct the parts of the SciRi detector in such a short amount of time. Also thanks to Paul Zuege and Patrick Bauer for the assistance during the detector assembly. I would also like to thank Daniel Hammann for the support in the implementation of the SciRi detector into the BGO-OD setup. Last but not least I thank Dr. Francesco Messi for advises concerning signal processing of SciRi.
For the strong support on the ExPlORA framework I would like to thank Oliver Freyermuth, who helped me in almost all ExPlORA problems I encountered. I would like to thank Dr. Tom Jude for his advise on analysis and for being my supervisor. Also thanks to Dr. Valentina Vegna, Dr. Giuseppe Mandaglio and Prof. Paolo Levi Sandri how were open for questions concerning the analysis.

APPENDIX A

Appendix

APD ID	Bais Voltage / V	Break. Voltage / V	a	b / V	c	d
105000259	339	380	-34,1766	381,8187	-4,2567	-2,4141
105000278	337,7	377	-15,3504	380,5664	-1,9788	-8,9698
105000284	340,4	378	-18,6402	383,2735	-2,352	-8,0082
105000292	341,4	384	-75,3564	387,8219	-8,0512	5,3082
105000311	339,4	379	-51,277	384,2814	-5,7493	0,4404
105000312	336,3	378	-18,0677	377,8138	-2,4028	-6,6932
105000356	355,4	400	-17,7416	402,1545	-2,2295	-7,8842
105000369	353,9	398	-71,0861	403,928	-6,9966	3,298
105000380	347	387	-61,404	393,6449	-6,5845	2,3128
105000392	357,7	402	-18,5318	404,812	-2,308	-7,7719
201000403	371,7	412	-68,1079	422,1128	-7,5072	5,0947
201000406	383,8	425	-54,8149	430,4691	-6,6965	4,4491
308000957	384,1	429	-63,5635	433,5541	-7,5858	5,3093
309000972	382,2	429	-16,6003	429,7745	-2,2968	-6,0102
309000976	380,8	426	-16,5358	427,7607	-2,3471	-5,5757
309000980	381,9	428	-16,4202	429,4911	-2,2738	-6,1172
309000991	379,8	425	-57,1035	428,8215	-6,7635	3,9204
309000992	381,4	424	-43,7562	429,9071	-5,5859	1,5824
309000996	383,1	428	-65,7864	432,441	-7,8549	5,9684
309001007	383,6	429	-55,43	432,7062	-6,6804	3,4727
309001010	375,8	420	-47,6468	423,6812	-5,5764	0,4527
309001012	378,7	425	-62,9726	428,4132	-7,2262	4,4982
310001029	389,3	435	-54,2657	437,9745	-6,7776	3,9011
310001033	384,1	427	-69,6058	434,0324	-7,67	4,9494
310001044	385,9	431	-48,9748	437,9511	-6,315	3,2278
310001061	391,5	437	-55,4796	440,2316	-6,9429	4,1588
310001071	390,8	437	-53,7981	439,6427	-6,6875	3,5001
310001078	386,6	428	-67,0784	435,9424	-7,6859	5,6459
310001087	386,2	429	-38,5482	433,2192	-4,9898	0,558
311001121	376	421	-16,5484	422,812	-2,2693	-6,4137
311001129	378,7	423	-16,7846	425,774	-2,3357	-5,9742
311001133	378,4	424	-16,9105	425,0195	-2,3693	-5,7437

Table A.1: Used APD parameter Part 1.The $Gain = \frac{a}{1-\frac{U}{b}^c} + d$ is only measured up to gain 50.[22]

APD ID	Bais Voltage / V	Break. Voltage / V	a	b / V	c	d
319001545	389	435	-0,7556	436,3587	-0,1006	-13,3369
320001563	385,8	431	-51,5054	435,1051	-6,4447	3,1601
321001609	383,4	429	-57,772	432,3816	-7,1311	4,6948
322001668	381,3	424	-17,0207	428,5812	-2,3665	-5,9922
322001701	383,9	429	-53,4094	433,1703	-6,6228	3,6612
323001795	383,4	426	-18,0408	430,6828	-2,5466	-5,4304
324001814	393,1	439	-18,0165	441,0332	-2,4483	-5,9966
324001880	394,7	441	-71,1576	445,5411	-8,0745	6,2675
325001899	381,8	424	-85,3346	441,965	-6,8653	0,1586
325001906	386,2	432	-17,0196	433,421	-2,3706	-5,8106
325001911	382,5	428	-70,527	430,8455	-8,1827	6,4637
325001912	393,8	440	-0,4752	438,4272	-0,0779	-9,0879
325001914	394,8	440	-26,4599	438,6951	-4,1441	0,7663
325001916	393	438	-51,7457	440,6465	-6,686	4,1334
325001922	387,8	434	-49,3709	436,5261	-6,2226	2,9723
325001923	394,3	440	-17,7557	441,6803	-2,5083	-5,6103
325001926	389,8	435	-19,9707	436,0159	-2,8798	-4,1179
325001936	393,8	438	-57,1044	443,3536	-7,0184	3,8261
325001943	395	441	-19,3883	441,779	-2,7475	-5,3336
325001945	389,1	435	-61,0238	439,1678	-7,1449	4,019
325001946	393,8	440	-0,2424	442,7968	-0,0299	-18,3509
326001956	388,6	429	-0,6903	431,9009	-0,1116	-9,693
326001963	383,7	427	-18,6777	431,0028	-2,594	-5,5409
326001971	383,2	426	-53,8117	430,9706	-6,8897	4,6997
326001973	389	434	-26,2418	446,358	-2,455	-16,6867
326001982	384,1	431	-17,4762	431,3356	-2,4363	-5,1875
327002035	384,6	429	-46,9431	433,0719	-6,0469	2,7277
327002041	382,6	424	-21,4285	429,9798	-2,9234	-4,9013
327002054	378,8	424	-17,8721	426,8794	-2,3539	-7,2893
328002159	391,5	436	-63,941	441,535	-7,6974	5,3811
328002169	383,4	428	-55,2502	432,3595	-6,8498	4,0806
329002194	394,2	439	-0,5065	437,318	-0,0868	-8,8275
329002197	392,7	439	-66,6015	441,9195	-7,9083	5,7227
329002209	380,6	426	-17,5238	428,3342	-2,4449	-5,6564
329002219	389,8	436	-17,1779	436,5359	-2,5027	-5,0964
334002491	388,9	435	-18,0384	435,6479	-2,4135	-5,8806
335002578	385,1	431	-15,1917	432,8796	-2,0608	-6,7324
336002658	387,9	433	-41,1057	435,7331	-5,4571	1,7415
336002685	387,2	433	-16,3789	433,0394	-2,3262	-5,1197
336002686	385,3	432	-43,196	434,2561	-5,4847	1,5877

Table A.2: Used APD parameter Part 2.The $Gain = \frac{a}{1-\frac{U}{b}^c} + d$ is only measured up to gain 50.[22]

APD ID	Bais Voltage / V	Break. Voltage / V	a	b / V	c	d
337002690	390,1	435	-17,9928	436,3677	-2,4656	-5,421
338002802	383,6	429	-17,8339	430,1337	-2,4792	-5,7406
339002849	391	437	-18,9759	444,2448	-2,1384	-11,0615
339002870	391,9	438	-71,5426	445,4582	-7,1314	3,1744
339002873	387	429	-0,0416	401,5322	-0,0363	17,814
343003151	383,1	428	-16,3492	429,6342	-2,3391	-5,6304
344003222	383,4	427	-115,5519	436,1235	-10,2248	7,9174
345003246	393,1	439	-19,834	439,7682	-2,7709	-4,213
345003256	393,7	439	-17,416	440,4193	-2,3611	-5,9934
345003265	394,9	440	-16,3643	440,9139	-2,2826	-5,8499
345003279	391,5	437	-58,3023	440,0404	-7,1954	5,1464
345003281	390,2	431	-71,5871	441,4096	-8,3018	6,1557
346003290	390,3	436	-16,2094	437,4407	-2,3027	-5,736
346003307	391,9	436	-16,5244	438,3342	-2,3884	-5,6372
346003313	388,3	435	-36,907	436,3202	-4,5524	-0,8899
346003333	391,9	438	-63,5627	441,5674	-7,634	5,285
346003337	389,3	435	-23,9071	436,2825	-3,3533	-2,9496
347003349	391,5	437	-65,5263	441,5077	-7,5873	5,1693
348003390	387,3	434	-19,4568	433,8247	-2,667	-4,6098
405003568	384	431	-0,0756	401,4328	-0,0612	19,0696
502004149	377,5	419	-40,4993	425,5635	-5,0787	0,353
503004201	380,1	424	-37,1436	427,2046	-4,9365	0,3834
503004217	379,6	425	-59,6493	429,3484	-7,0556	4,266
601004236	408,3	453	-17,2724	454,4567	-2,4953	-4,9766
601004261	409,6	455	-18,9439	456,6812	-2,7343	-5,2136
601004263	406,6	451	-17,8444	453,2211	-2,5094	-6,0202
601004268	409,1	451	-51,37	457,6508	-6,7434	3,2666
601004276	403	448	-54,4492	451,1657	-7,0008	4,0783
602004300	405,9	452	-18,6406	452,4458	-2,7617	-4,6182
605004479	403,1	446	-19,3183	449,764	-2,9215	-4,1584

Table A.3: Used APD parameter Part 3.The $Gain = \frac{a}{1-\frac{U}{b}^c} + d$ is only measured up to gain 50.[22]

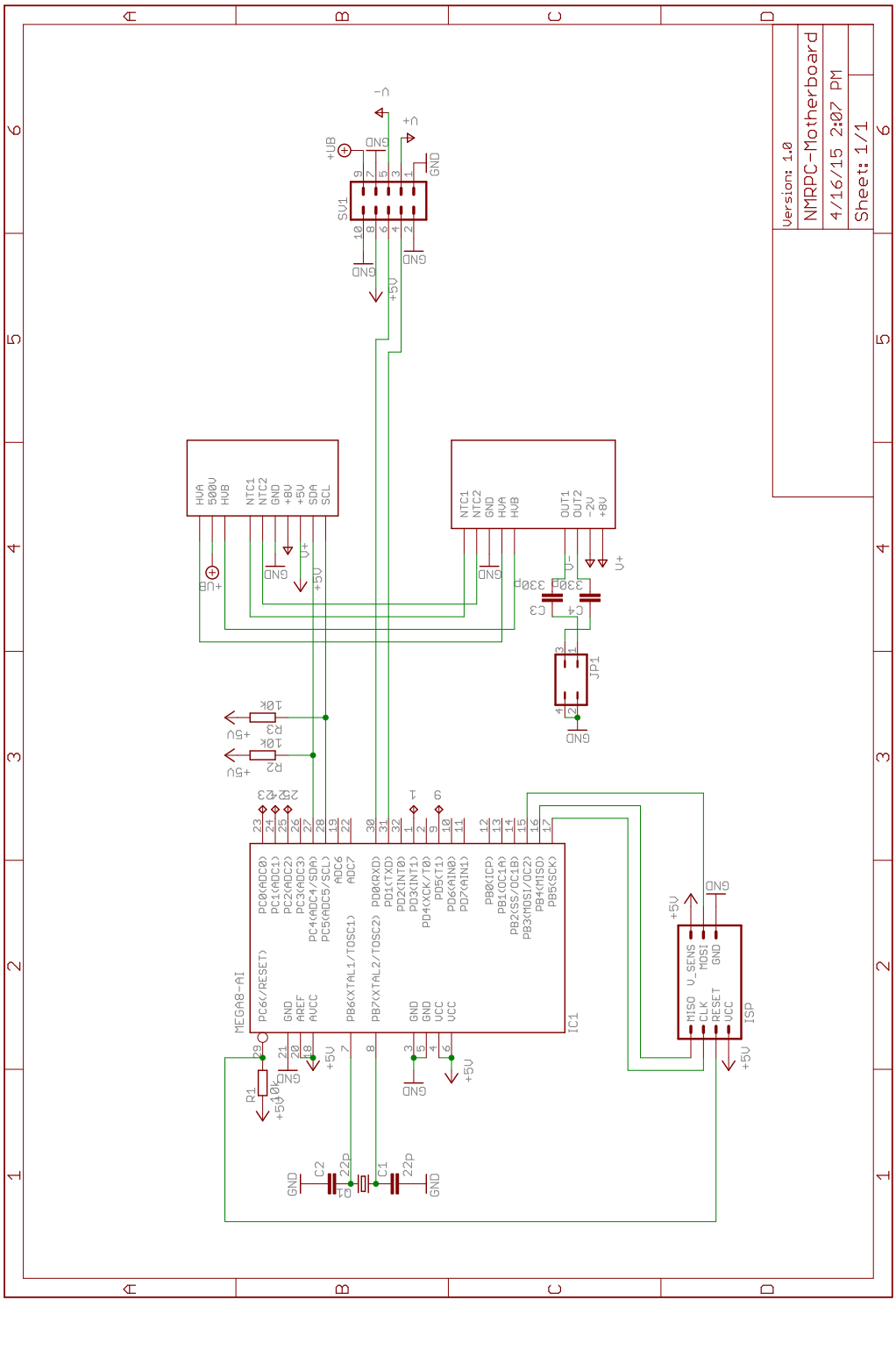

Figure A.1: Electronic circuit of the SciRi Mainboard [26]

HV board ID	Poti 1 s / V	Poti 1 c / V	Poti 2 s / V	Poti 2 c / V
8441097	-0.127122	466.117	-0.127019	466.276
8441746	-0.1271102	466.552	-0.127445	466.138
8446226	-0.1274417	466.256	-0.12713	465.987
8446438	-0.127393	465.931	-0.127039	466.196
8447041	-0.1272262	466.822	-0.127526	466.217
8447118	-0.1258357	466.622	-0.126187	466.234
8447368	-0.1278287	466.21	-0.12675	466.065
8447502	-0.1277048	466.65	-0.127629	466.485
8452587	-0.1271486	466.492	-0.127425	466.157
8452610	-0.1271068	466.163	-0.127268	466.049
8453487	-0.1274693	466.389	-0.126818	466.114
8459951	-0.1276487	466.387	-0.127194	466.341
8459985	-0.1271147	466.244	-0.12752	466.045
8460263	-0.127345	466.252	-0.127927	466.175
8460340	-0.1271877	466.177	-0.126771	466.097
8461433	-0.127536	466.48	-0.126901	466.578
8461592	-0.1274529	466.266	-0.127444	466.156
8461901	-0.1267455	466.013	-0.126782	465.974
8462012	-0.1271898	466.204	-0.127126	466.227
8462148	-0.1270202	466.088	-0.126678	466.203
8462253	-0.1281788	466.158	-0.126934	466.126
8462333	-0.1275956	466.309	-0.127055	466.292
8467879	-0.1273071	466.159	-0.127414	465.934
8467994	-0.1271103	466.174	-0.126889	465.923
8468114	-0.1274552	466.311	-0.126896	466.674

Table A.4: Voltage ↔ Poti setting relation for the HV Boards [22]. $U = s \cdot Potivalue + c$. Part 1

HV board ID	Poti 1 s / V	Poti 1 c / V	Poti 2 s / V	Poti 2 c / V
8468820	-0.1272831	466.444	-0.127393	466.327
8468840	-0.1269955	466.011	-0.127364	466.021
8469165	-0.1277045	465.891	-0.127017	466.115
8469438	-0.1275372	466.28	-0.128244	466.147
8469539	-0.1282609	466.167	-0.128368	465.92
8469861	-0.1279762	466.217	-0.126311	466.327
8470273	-0.1276033	466.24	-0.127958	465.88
8470357	-0.1278712	466.33	-0.126971	466.318
8470364	-0.1269079	466.236	-0.127128	465.964
8475453	-0.1279192	466.471	-0.127861	466.143
8475560	-0.1265329	466.753	-0.126204	466.2
8475624	-0.1274709	465.953	-0.127466	466.1
8476034	-0.1269027	466.42	-0.126568	466.12
8476481	-0.1272151	465.862	-0.126774	465.768
8482591	-0.1282911	466.146	-0.128159	466.108
8482748	-0.1269917	466.258	-0.127609	465.77
8482902	-0.1271703	466.232	-0.127088	465.945
8483290	-0.1279994	466.351	-0.127428	466.471
8483500	-0.127417	466.196	-0.127912	465.888
8483801	-0.1270578	466.149	-0.126427	466.2
8483899	-0.126808	466.3	-0.128079	465.7
8484055	-0.127466	466.337	-0.126478	466.078
8484161	-0.1280334	466.657	-0.127495	466.466
8488416	-0.1278093	466.32	-0.127653	466.173
8488508	-0.128823	466.107	-0.127973	465.917

Table A.5: Voltage ↔ Poti setting relation for the HV Boards [22]. $U = s \cdot Potivalue + c$. Part 2

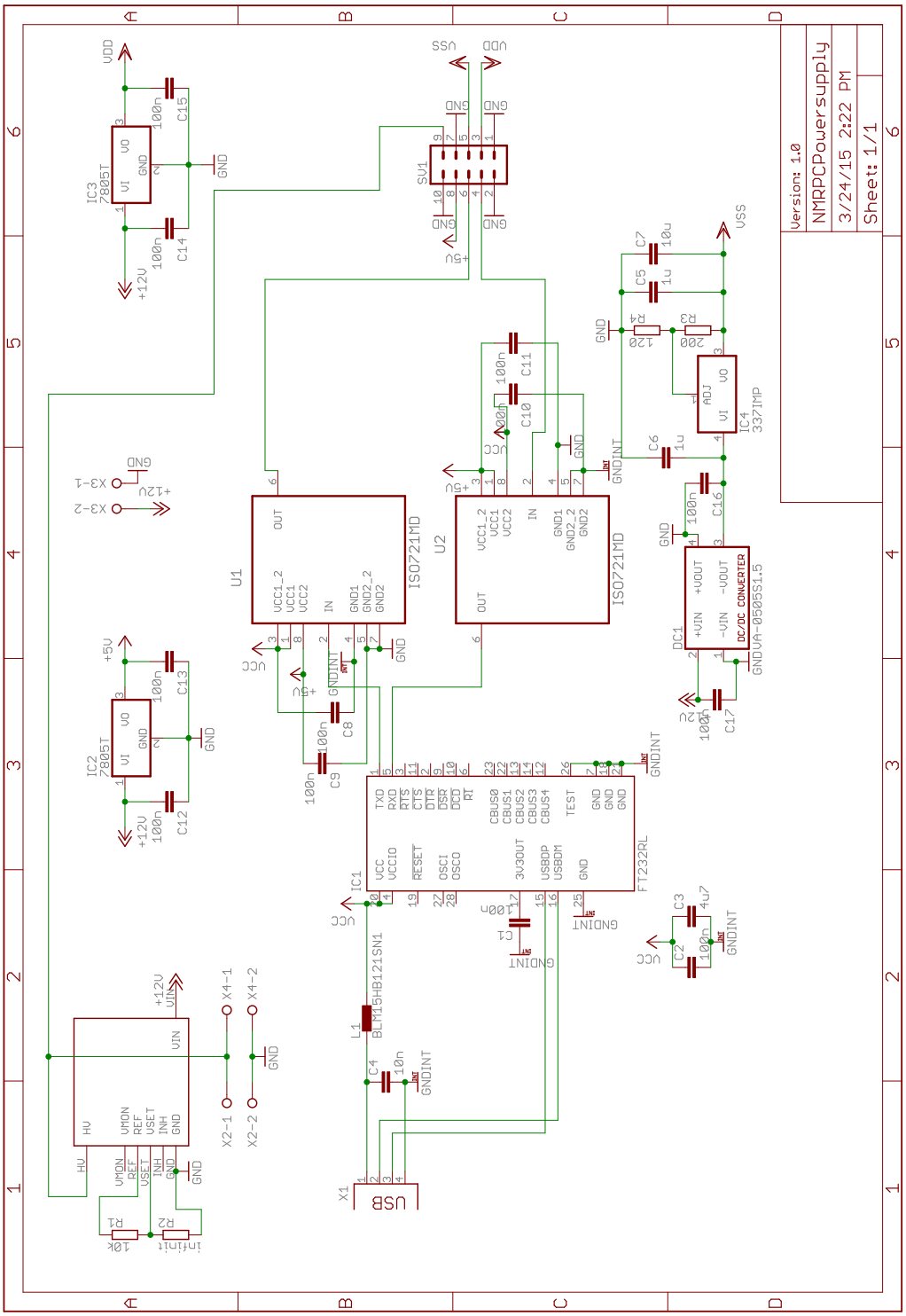

Figure A.2: Electronic circuit of the SciRi Voltage Supply Board [26]

Bibliography

[1] *STONY BROOK, Hadron Collider Experiments: DØ and ATLAS*, URL: http://sbhep-nt.physics.sunysb.edu/HEP/AcceleratorGroup/index.html (cit. on p. 1).

[2] N. et al., *Physical Review C*, 4th ed., Volume 54,Number 4, October 1996 (cit. on p. 2).

[3] *Electron Stretcher Accelerator (ELSA) Homepage*, URL: http://www-elsa.physik.uni-bonn.de/index_en.html (cit. on p. 5).

[4] J. Hannappel, *Private communication*, BGO-OD Experiment (cit. on p. 6).

[5] F. Messi, *The tagging system of the BGO-OD experiment*, doctoral thesis, Juli 2015 (cit. on p. 7).

[6] B.-E. Reitz, *Construction of an additional hodoscope for the BGO-OD experiment consisting of scintillator fibres (ARGUS) together with simple π^0 analysis*, Master thesis, Estimated to be ready at the end of 2015 (cit. on p. 7).

[7] S. Alef, *Development of a scintillating fibre hodoscope (ARGUS) for the tagging system of the BGO-OD experiment*, Master thesis, Estimated to be ready at the end of 2015 (cit. on p. 7).

[8] B. Leibrock, *Erstinbetriebnahme der Vieldrahtproportionalkammer des BGO-OD-Experiments*, Bachelor thesis, September 2014 (cit. on p. 8).

[9] M. Becker, *Charakterisierung eines MRPC-Prototypdetektors für das BGO-OD Experiment*, Bachelor thesis, September 2014 (cit. on p. 9).

[10] S. Böse, *Aufbau und Test eines neuen Szintillationsfaser-Detektors für das neue Vorwärtsspektrometer an ELSA*, doctoral thesis, 2015 (cit. on p. 9).

[11] T. Frese, *Insitu field measurement of the Open Dipole magnet at the BGO-OD experiment*, Master thesis, December 2012 (cit. on p. 9).

[12] T. Schwan, *Test und Inbetriebnahme der Driftkammern für das BGO-OD-Spektrometer*, Diplomarbeit, April 2010 (cit. on p. 9).

[13] P. Meiß, *The Time Of Flight Spectrometer of the BGO-OD Experiment*, Diplomarbeit, September 2013 (cit. on p. 9).

[14] U. Thoma et al., *ExPlORA, Extended Plugable Objectoriented ROOT Analysis*, Version 1.3 (cit. on pp. 11, 41).

[15] *ROOT Homepage, Data Analysis Framework*, URL: https://root.cern.ch (cit. on p. 11).

[16] S. Agostinelli et al., *Geant4—a simulation toolkit*, Nuclear Instruments and Methods in Physics Research A, Volume 506, Issue 3, 1 July 2003 (cit. on p. 11).

[17] *Particle Physics Booklet*, Particle Data Group, 2012 (cit. on pp. 11, 33, 37, 38, 42, 45, 47).

[18] *Radioisotopes and Radiation Methodology, Chapter 4*, URL: https://graduate.mcmaster.ca/medphys/images/files/courses/4R06/note4.pdf (cit. on pp. 18, 19).

[19] W. R. Leo, *Techniques for nuclear and particle physics experiments: a how-to approach*, Springer, 1994 (cit. on p. 19).

[20] G. F. Knoll, *Radiation Detection and Measurement*, 3rd ed., John Wiley & Sons, Inc, (cit. on pp. 19, 24).

[21] M. Urban, C. Honisch and M. Steinacher, *The New APD Based Readout for the Crystal Barrel Calorimeter*, IOPscience, 16th International Conference on Calorimetry in High Energy Physics (CALOR 2014), Journal of Physics: Conference Series 587 (2015) 012043, 2015 (cit. on pp. 24, 25).

[22] M. Urban, *Private communication*, Crystal Barrel Experiment (cit. on pp. 24, 25, 61–63, 65, 66).

[23] I. Keshelashvili et al., *Development of Low-Noise/Low-Power Preamplifier for the Readout of Inorganic Scintillators and their Mass Production Test System*, IOPscience, 16th International Conference on Calorimetry in High Energy Physics (CALOR 2014), Journal of Physics: Conference Series 587 (2015) 012024, 2015 (cit. on pp. 25, 26).

[24] *Crystal Barrel Experiment Homepage*, URL: www.cb.uni-bonn.de (cit. on p. 25).

[25] C. Honisch, *Private communication*, Crystal Barrel Experiment (cit. on pp. 25, 26).

[26] T. Zimmermann, *Private communication*, BGO-OD Experiment (cit. on pp. 26, 28, 64, 67).

[27] J. Bieling, *jTDC: a high resolution FPGA based TDC*, URL: https://github.com/jobisoft/jTDC (cit. on p. 29).

[28] P. Züge, *Aufbau und Test eines segmentierten Plastic Scintillator Ring Detector für das BGO-OD Experiment*, Bachelor thesis, Estimated to be ready at the end of 2015 (cit. on p. 33).

[29] *Picture of an electromagnetic shower*, URL: https://en.wikipedia.org/wiki/Particle_shower#/media/File:Schematic_of_a_particle_shower.svg (cit. on p. 42).

[30] W. Allison, *Fundamental Physics for Probing and Imaging*, Oxford University Press Inc. New York, 2006 (cit. on p. 42).

[31] T. Jude, *Private communication*, BGO-OD Experiment (cit. on p. 42).

[32] A. Zucchiatti et al., *Optimisation of cluster algorithms for the reconstruction of events started by a 1 GeV photon beam in a segmented BGO calorimeter*, Nuclear Instruments and Methods in Physics Research A, 24 September 1998 (cit. on p. 44).

List of Figures

List of Tables